

Universidade Federal de Juiz de Fora  
Instituto de Ciências Exatas / Faculdade de Engenharia  
Programa de Pós-Graduação em Modelagem Computacional

**Evandro Dias Gaio**

**Numerical simulations for blood flow problems using Fluid-Structure  
Interaction with stabilized finite element methods**

Juiz de Fora

2019

**Evandro Dias Gaio**

**Numerical simulations for blood flow problems using Fluid-Structure  
Interaction with stabilized finite element methods**

Dissertação apresentada ao Programa de Pós-Graduação em Modelagem Computacional da Universidade Federal de Juiz de Fora, como requisito parcial para obtenção do título de Mestre em Modelagem Computacional.

Orientador: Rafael Alves Bonfim de Queiroz

Coorientador: José Jerônimo Camata

Juiz de Fora

2019

Ficha catalográfica elaborada através do Modelo Latex do CDC da UFJF  
com os dados fornecidos pelo(a) autor(a)

Dias Gaio, Evandro.

Numerical simulations for blood flow problems using Fluid-Structure Interaction with stabilized finite element methods / Evandro Dias Gaio. – 2019.

69 f. : il.

Orientador: Rafael Alves Bonfim de Queiroz

Coorientador: José Jerônimo Camata

Dissertação (Mestrado) – Universidade Federal de Juiz de Fora, Instituto de Ciências Exatas / Faculdade de Engenharia. Programa de Pós-Graduação em Modelagem Computacional, 2019.

1- Escoamento sanguíneo, 2- Vasos sanguíneos deformáveis, 3- Interação Fluido-Estrutura, 4- Método dos Elementos Finitos, 5- FEniCS. I. Alves Bonfim de Queiroz, Rafael, orient. II. Jerônimo Camata, José, coorient. III. Título.

Evandro Dias Gaio

**Numerical simulations for blood flow problems using Fluid-Structure  
Interaction with stabilized finite element methods**

Dissertação apresentada ao Programa de Pós-Graduação em Modelagem Computacional da Universidade Federal de Juiz de Fora, como requisito parcial para obtenção do título de Mestre em Modelagem Computacional.

Aprovada em: 12/09/2019

BANCA EXAMINADORA

---

Prof. Dr. Rafael Alves Bonfim de Queiroz - Orientador  
Universidade Federal de Juiz de Fora

---

Professor Dr. José Jerônimo Camata - Coorientador  
Universidade Federal de Juiz de Fora

---

Professor Dr. Renato Nascimento Elias  
Universidade Federal do Rio de Janeiro

---

Professor Dr. Iury Higor Aguiar da Igreja  
Universidade Federal de Juiz de Fora

## AGRADECIMENTOS

Aos meus orientadores, Dr. Rafael Alves Bonfim de Queiroz e Dr. José Jerônimo Camata, pela orientação, conversas, paciência e apoio para o desenvolvimento deste trabalho.

À minha família, por todo apoio e compreensão.

Aos amigos do Programa de Pós-graduação em Modelagem Computacional, pela agradável convivência, que renderam muitas risadas e histórias e também pelo suporte ao longo da realização deste trabalho.

À todas as pessoas que de alguma forma contribuíram para a realização deste trabalho, seja de forma direta ou indireta, com apoio emocional e financeiro.

Ao PPGMC, à UFJF e à CAPES, pelo apoio financeiro direcionado à minha pesquisa.

“The purpose of computation is insight, not numbers”,

Richard Hamming.

## RESUMO

O estudo e simulação de escoamentos sanguíneos no sistema cardiovascular (*CS - Cardiovascular System*) tem muitas aplicações, como estudos de patologias, planejamento de cirurgias e projeto de dispositivos médicos. O escoamento sanguíneo no CS pode ser considerado um problema de dinâmica dos fluidos, e no caso ótimo, um problema acoplado entre dinâmicas dos sólidos e dos fluidos, chamado de problema de interação fluido-estrutura (*FSI - Fluid-Structure Interaction*). Esse trabalho primeiro foca na solução de diferentes problemas de dinâmica dos fluidos, usando diferentes estabilizações numéricas para a solução da equação de Navier-Stokes através do método de Galerkin. Uma comparação usando tempo de CPU e erros para diferentes níveis de refinamento da malha é feita, como forma de avaliar e explorar a plataforma FEniCS e a função dos termos estabilizadores. Esse método pode ser usado na simulação de escoamento sanguíneo que considera um domínio de parede rígida. Entretanto, alguns autores dizem que a velocidade de escoamento e pressão sanguínea são fortemente influenciadas pela dinâmica das paredes. Por essa razão, na segunda parte deste trabalho, foi utilizado o método de momento acoplado (*CMM-FSI - Coupled Momentum Method for FSI*) para resolver problemas de escoamento sanguíneo em artérias grandes e deformáveis. O *CMM-FSI* simplifica o processo de acoplamento fluido-estrutura quando utilizando o método dos elementos finitos devido a ser baseado em um acoplamento forte dos graus de liberdade nos domínios do fluido e do sólido. Isso pode ser feito acoplando a deformação da parede do vaso no nível variacional, como uma condição de contorno para o domínio do fluido e também mantendo a descrição de movimento (Euleriana) para uma malha fixa. A parte positiva do *CMM-FSI* é que demanda um esforço computacional muito menor, principalmente para modelos 3D, do que métodos Eulerianos-Lagrangiano arbitrários convencionais. Por outro lado, esse método pede que a ordem de aproximação polinomial dos elementos para pressão e velocidade sejam da mesma ordem. Dessa forma, uma formulação estabilizada de elementos finitos é usada. Toda a implementação numérica é feita usando Python e FEniCS, uma biblioteca de elementos finitos. Relações constitutivas de fluido Newtoniano e uma estrutura de parede fina são consideradas. Uma comparação é feita com a teoria de escoamento sanguíneo de Poiseuille e também com suposição de parede fixa. Os impactos de escolha da suposição de parede fixa e do modelo deformável são avaliados através de parâmetros hemodinâmicos, como picos de pressão durante a sístole e diástole e a velocidade de propagação de ondas do escoamento sanguíneo. Finalmente, o *CMM-FSI* é usado para realizar uma simulação em um modelo idealizado da artéria carótida comum com estenose. Os resultados obtidos neste trabalho estão condizentes com a literatura.

Palavras chaves: Escoamento sanguíneo, Vasos sanguíneos deformáveis, Interação Fluido-Estrutura, Método dos Elementos Finitos, FEniCS.

## ABSTRACT

The study and simulation of blood flow in the cardiovascular system (CS) have many applications such as pathologies studies, surgical planning, and design of medical devices. The blood flow in the CS can be considered as a fluid dynamics problem, and in the optimal case, a coupling between fluid and solid dynamics, named Fluid-Structure Interaction (FSI) problems. Firstly, this work focuses on solving different fluid dynamics problems using usual stabilizations for the Galerkin method in order to solve the Navier-Stokes equation. A comparison using CPU time and error for different levels of mesh refinement is made as a way to evaluate and explore the FEniCS library and the function of each stabilization term. This method may be used to perform blood flow simulations using a rigid wall domain assumption. However, some authors say that blood velocity and pressure in large arteries are greatly influenced by vessel wall dynamics. By this reason, in the second part of this work, it was used the Coupled Momentum Method of Fluid-Structure Interaction (CMM-FSI,) to solve blood flow problems in large arteries. The CMM-FSI simplifies the fluid-structure coupling process when using a finite element formulation due to be based on a strong coupling of degrees-of-freedom of the fluid and the solid domains. It could be made by coupling the vessel wall deformation at the variational level as a boundary condition for the fluid domain and by keeping the same description of motion (Eulerian) in both domains, and with a fixed mesh. One of the positive parts of CMM-FSI is that it demands a lot less computational effort, mainly for 3D models, than usual arbitrary Lagrangian-Eulerian methods. On the other hand, this method claims that the polynomial approximation of the pressure and velocity elements must be the same order. Thus, a stabilized finite element formulation is used. All numerical implementation is done using Python and FEniCS, a finite element library. Constitutive relationships of Newtonian fluid and thin-walled structure are considered. A comparison is made with Poiseuille's blood flow theory and also with a rigid wall assumption. The impacts of choosing a rigid wall assumption or a deformable model are evaluated with hemodynamics parameters, as pressure peaks in diastole and systole and blood flow wave velocities. Finally, the CMM-FSI is used to perform a blood flow simulation in an idealized common carotid with stenosis. The results obtained in this work are consistent with the literature.

Keywords: Blood flow, Deformable vessels, Fluid-Structure Interaction, Finite Element Method, FEniCS.

## LIST OF FIGURES

Figure 1 – Visualization of the aorta (left), carotids (middle) and coronaries (right). Taken from [1]. . . . .	20
Figure 2 – The time delay ( $\Delta t$ ) due the pressure wave travelling from the ascending aorta (red) to the femoral artery (blue). Taken from [2]. . . . .	21
Figure 3 – The blood vessel simplified anatomy. Modified from [3]. . . . .	22
Figure 4 – The common carotid artery divides into the internal and external carotid arteries. Source: [4]. . . . .	23
Figure 5 – Simplified illustration of the main blood composition. Source: [5]. . . . .	23
Figure 6 – Molecular distribution in a fluid particle. Source: [6]. . . . .	25
Figure 7 – Stress of a typical membrane patch with transverse shear. Taken from [7].	29
Figure 8 – Schematic representation of the fluid and solid domains and their boun- daries. Adapted from [7]. . . . .	30
Figure 9 – Flow chart of PDE to linear/nonlinear system. . . . .	33
Figure 10 – Main free software and open source codes used by FEniCS. (a) the flow chart of a FEniCS program. (b) the external libraries that FEniCS carries in. Adapted from [8]. . . . .	40
Figure 11 – Schematic overview of the most important components and classes of DOLFIN. Arrows indicate dependencies [8]. . . . .	41
Figure 12 – Numerical simulation result of driven cavity problem at $t = 2.5$ with $Re=1000$ . . . . .	44
Figure 13 – Simulation analysis of driven cavity problem. . . . .	44
Figure 14 – Numerical results of the pressure driven problem at $t = 0.5$ . . . . .	45
Figure 15 – Simulation analysis of the pressure driven problem. . . . .	46
Figure 16 – Initial conditions of the taylor-Green vortex problem [8]. . . . .	47
Figure 17 – Numerical simulations of Taylor-Green vortex problem at $t = 0.5$ . . . . .	47
Figure 18 – Simulation analysis of Taylor-Green Vortex problem. . . . .	48
Figure 19 – Flow past a cylinder geometry. . . . .	48
Figure 20 – Stream line simulation result of flow around a cylinder problem. . . . .	49
Figure 21 – Pressure simulation result of flow around a cylinder problem. . . . .	50
Figure 22 – Simulation analysis of flow around a cylinder problem. . . . .	50
Figure 23 – Mesh visualization of an idealized vessel. . . . .	52
Figure 24 – Comparisons between rigid and deformable models against theoretical function. . . . .	53
Figure 25 – Wall displacement. . . . .	54
Figure 26 – Mesh visualization for idealized common carotid. . . . .	55

Figure 27 – Sinusoidal model: Pressure and velocity for 2 cycles. . . . .	55
Figure 28 – Planes S1 and S2 of evaluation. Adapted from [7]. . . . .	56
Figure 29 – Pressure and blood flow waves at the outlet an inlet faces, respectively. 1 cc = $10^{-6} m^3$ . . . . .	56
Figure 30 – Comparison between rigid and deformable models. Plots (a) and (b) are the flow overtime for a pressure wave and fixed pressure respectively. Plots (c) and (d) are the pressure overtime for pressure wave BC and fixed pressure respectively. . . . .	58
Figure 31 – Radial displacement in S1 and S2 for the carotid artery model using constant pressure BC and pressure wave BC. . . . .	59
Figure 32 – Stenosis geometry of the carotid artery. . . . .	59
Figure 33 – Stenosis mesh for the carotid artery model. . . . .	59
Figure 34 – Simulation result of the common carotid artery with stenosis. The results are pressure, blood velocity and wall velocity from top to bottom. . . . .	61

## LIST OF ACRONYMS

ALE	Arbitrarian-Lagrangian- Eulerian
BC	Boundary Condition
CD	Cardiovascular Disease
CFD	Computational Fluid Dynamics
CMM-FSI	Coupled Momentum Method for Fluid-Structure Interaction
CS	Cardiovascular System
FEM	Finite Element Method
FFC	FEniCS form compiler
FSI	Fluid-Structure Interaction
LBB	Ladyzhenskaya–Babuška–Brezzi
LSIC	Least-Squares on Incompressibility Constraint
NSE	Navier-Stokes Equations
PDEs	Partial Diferential Equations
PSPG	Pressure-Stabilizing/Petrov-Galerkin
PWV	Pulse Wave Velocity
SUPG	Streamline-Upwind /Petrov-Galerkin
UFC	Unified form assembly
UFJF	Universidade Federal de Juiz de Fora
UFL	Unified Form Language

## LIST OF SYMBOLS

$E$	Young's modulus
$\mathbf{h}$	Prescribed Neumann condition
$\mathbf{g}$	Prescribed Dirichlet condition
$D$	Vessel diameter
$Re$	Reynolds Number
$p$	Fluid Pressure
$\mathbf{u}$	Fluid velocity
$\bar{I}$	Identity tensor
$\mathbf{f}$	Total external forces acting in the fluid
$\bar{\mathbf{C}}$	Fourth-order tensor of material stiffness
$\bar{\mathbf{D}}$	Second-order tensor of material stiffness
$F_v$	Total external forces acting in the solid
$\mathbf{v}$	Displacement
$\dot{\mathbf{v}}$	Solid velocity
$\ddot{\mathbf{v}}$	Solid acceleration
$H^1$	Hilbert space
$\mathbf{w}$	Velocity test function
$q$	Pressure test function
$U$	Mean velocity
$\rho$	Density
$\rho^f$	Fluid density
$\rho^s$	Solid density
$\dot{\rho}$	Change of density overtime
$\mu$	Dynamic viscosity
$\nu$	Kinematic viscosity

$\bar{\sigma}$	Stress Tensor
$\bar{\sigma}_1$	Internal pressure stress tensor
$\bar{\sigma}_2$	Viscous stress tensor
$\bar{\sigma}^f$	Fluid stress tensor
$\bar{\sigma}^s$	Solid stress tensor
$\dot{\mathbf{u}}$	Fluid acceleration
$\bar{\epsilon}$	Strain Tensor
$\Gamma_g$	Inlet boundary
$\Gamma_h$	Outlet boundary
$\Gamma_s$	Solid-fluid interface boundary
$\partial\Gamma$	Wall boundary
$\zeta$	Wall thickness
$\Omega$	Domain
$\Omega^f$	Fluid domain
$\Omega^s$	Solid domain
$\partial\Omega_D$	Dirichlet boundary condition
$\partial\Omega_N$	Neumann boundary condition
$\phi$	Basis function
$\tau$	Stabilization parameter
$\forall$	For all
$\in$	Belongs
$\mathcal{R}$	Residual of momentum
$\mathcal{P}$	A particular operator

## SUMMARY

<b>1</b>	<b>INTRODUCTION</b>	<b>15</b>
1.1	MOTIVATION	17
1.2	OBJECTIVE	17
1.3	STRUCTURE	18
<b>2</b>	<b>ARTERIAL CIRCULATION</b>	<b>19</b>
2.1	CARDIOVASCULAR SYSTEM	19
2.1.1	Blood pressure and arterial stiffness	19
2.1.2	Blood pulse wave and wave reflection phenomena	20
2.1.3	Large Vessels	21
2.1.4	Carotid artery	22
2.2	BLOOD	23
<b>3</b>	<b>MATHEMATICAL MODELING</b>	<b>24</b>
3.1	FLUID MECHANICS	24
3.1.1	Mass conservation	25
3.1.2	Momentum balance	25
3.1.3	Constitutive relationship for blood flow problems	26
3.1.4	Newtonian fluid	26
3.1.5	The Navier-Stokes equations	27
3.2	SOLID MECHANICS: LINEAR ELASTICITY	27
3.2.1	Constitutive relationship for blood vessel mechanics	28
3.2.2	Thin-walled structure	28
3.2.3	Initial, boundary and interface conditions	30
3.3	FLUID STRUCTURE INTERACTION	31
<b>4</b>	<b>NUMERICAL METHODS</b>	<b>33</b>
4.1	FINITE ELEMENT METHOD	33
4.2	FLUID PROBLEM DISCRETIZATION	33
4.2.1	Galerkin formulation	34
4.2.2	Stabilizations for Galerkin Formulation	34
4.2.2.1	Streamline-Upwind/Petrov-Galerkin	35
4.2.2.2	Pressure-Stabilizing/Petrov-Galerkin	35
4.2.2.3	Least-Squares on Incompressibility Constraint	36
4.3	SOLID DISCRETIZATION	36
4.3.1	Galerkin approximation	37

4.4	Combined formulation: CMM-FSI . . . . .	38
4.4.1	Method to find the deformation . . . . .	38
4.5	ALGORITHM OF THE CMM-FSI . . . . .	39
<b>5</b>	<b>NUMERICAL INVESTIGATION FOR FLUID PROBLEMS</b>	<b>40</b>
5.1	THE FEniCS LIBRARY . . . . .	40
5.2	FLUID PROBLEMS BENCHMARKS . . . . .	42
5.2.1	Driven Cavity . . . . .	43
5.2.2	Pressure Driven . . . . .	45
5.2.3	Taylor-Green vortex . . . . .	46
5.2.4	Flow past a cylinder . . . . .	48
5.2.5	Conclusions on FEniCS for fluid problems . . . . .	51
<b>6</b>	<b>ARTERIAL BLOOD FLOW</b> . . . . .	<b>52</b>
6.1	FLUID-STRUCTURE MODEL VALIDATION . . . . .	52
6.2	BLOOD FLOW AND PRESSURE WAVES . . . . .	54
6.2.1	Rigid versus deformable model: a comparative study . . . . .	56
6.3	FLOW IN A STENOSED COMMON CAROTID ARTERY . . . . .	59
<b>7</b>	<b>CONCLUSION</b> . . . . .	<b>62</b>
	<b>REFERENCES</b> . . . . .	<b>64</b>

## 1 INTRODUCTION

The Computational Fluid Dynamics (CFD) is an area of mathematics and branch of fluid mechanics that are used in the design of many systems [9]. CFD for incompressible flow focuses on solving the Navier-Stokes equations (NSE), named in honor of the studies of the engineer and physicist Claude Louis Marie Henri Navier and the mathematician and physicist George Gabriel Stokes, which describes the motion of viscous fluid particles, based on the conservation of mass and momentum.

Incompressible fluid dynamics and so on the NSE are significant in many areas of knowledge. They are used in computational modeling of climate change, pipeline flow, aircraft projects, blood flow studies, and many other applications [10]. In some applications, the fluid exerts interactions with another medium, and vice versa, for example, airfoil, aircraft, and blood flow projects in which the fluid interacts with a solid, falling into so-called fluid-structure interaction (FSI) problems [11].

Multiphysics problems are present in most of the natural phenomena in the world. For FSI problems, they are present in fields such as the design of wind-turbines, parachutes, aircraft, bridges, and many more [11, 12, 13]. It is also present in bioengineering, biomedical and cardiovascular area [7, 9, 14, 15, 16, 17]. Those problems are characterized as partial differential equations with boundary conditions related to both domains or physics (fluid and solid). It is really difficult to search for analytical solutions [11]. Thus, significant advances in research of computational methods have been developed in the last decades, especially applications in problems of fluid mechanics and fluid-structure interaction [7, 11, 18, 19, 20, 21].

One of the most used approaches to include deformation of the vessel wall is the Arbitrary-Lagrangian-Eulerian (ALE) [22, 23] formulation to solve FSI problems. However, this technique encounters significant challenges for three-dimensional blood flow modeling, since it needs for the fluid and structure, to update the geometry at each step of time, resulting in an expensive approach. Besides, some physiological applications require long simulation time [7]. In this way, the search for methods to incorporate wall deformation is essential for these applications.

The Coupled Momentum Method for Fluid-Structure interaction (CMM-FSI) proposed by Figueroa *et al.* [7, 24] in order to avoid some difficulties found in the ALE method. The CMM-FSI considers the conventional formulation of finite elements for the Navier-Stokes equations in a rigid domain, adding modifications in such a way that the deformation of the membrane is considered. It is based on the idea that the diameters of the arteries are small when compared to the wavelength of the cardiac pulse, causing the solid to exhibit a membrane over the bend, requiring no additional degrees of freedom in the wall of the solid. Thus, the linear membrane is reinforced with transverse shear, as

discussed in [25].

The CMM-FSI is traditionally used for hemodynamics since this model enables a pure fluids code to be generalized to include wave propagation and represents a computationally efficient alternative to ALE formulations for modeling blood flow in large deformable models of the vasculature. However, CMM-FSI will not produce results that are equivalent to ALE since, in its current implementation, it is utilized a fixed fluid mesh and linearized kinematics. Thus, the vessel wall constitutive equation needs to be expanded to consider anisotropy and to include viscoelastic effects to reproduce a more realistic simulation. This method also considers a fixed inlet and outlet rings of the vessel wall, which adds an artificial wave reflections on the structure.

Another important principle in blood circulation is the wave or pulsatile phenomena [26]. Developing and studying numerical models that represent the pulsatile phenomena in hemodynamics have many applications, such as surgical planning and design of medical devices [16]. For instance, Taylor and Figueroa [14] use the modeling of cardiovascular mechanics, involving fluid and solid behaviors for applications such as disease research and predictive medicine. To see the wave phenomena it is important to define impedance boundary conditions as an outflow so it can be compared with Womersley's linear wave theory. Using this linear wave propagation theory, the input impedance of the downstream vascular bed can be computed for large complex vascular trees [7].

The Finite Element Method (FEM) is already a consolidated method [27, 28] which has been used for decades in the area of numerical analysis, having a great prominence in the area of fluid mechanics [29]. The Galerkin's standard formulation for the incompressible Navier-Stokes equations, using interpolating polynomials of the same order, presents numerical instabilities since it does not satisfy the Ladyzhenskaya–Babuška–Brezzi (LBB) or inf-sup compatibility condition [30]. Thus, the stabilized formulation Streamline-Upwind / Petrov-Galerkin (SUPG) [31] for velocity, stabilized Pressure-Stabilizing/Petrov-Galerkin (PSPG) [32] for pressure and a catch term Least-Squares on Incompressibility Constraint (LSIC) [33] are used to make the CMM-FSI stable for every problem in this work.

For this work, all numerical implementation is done using Python and FEniCS library. FEniCS is a public domain library for the solution of differential equations based on the finite element method [8]. The development of this library began in 2003, to facilitate the automated solution of mathematical models. FEniCS is a comprehensive library of finite elements that include: automated error and adaptability controls, high-performance linear algebra, parallel computing, among other functionalities. The library allows effortless coding. The variational formulation is detailed in almost mathematical notation, including all kinds of variational form, which characterizes the generality of the library. FEniCS programs can be implemented in Python and C++ languages [34].

## 1.1 MOTIVATION

It is estimated that 17.9 million people died of cardiovascular disease (CD) in 2016, representing 31% of all deaths in the world. It is also known that of the 17 million premature deaths (people under 70) due to noncommunicable diseases in 2015, 37% are caused by CDs. Still, this number is expected to rise to over 23.6 million by 2030. In this scenario, it is still estimated that the overall cost of heart disease will exceed \$ 1044 billion by 2030 [35, 36]. Thus, heart and circulatory system diseases remain a challenge for healthcare systems around the world.

The blood flow is normal in healthy people, but individuals with specific pathologies are prone to abnormal flow, and the formation and development of aneurysms which are directly influenced by flow patterns in the arteries [37, 38]. However, many application studies of arterial models do not take into account the deformation of the vessel, assuming it as rigid [39, 40, 41]. By this reason, these hypotheses do not realistically represent the practices of these applications, because the deformation of the vessel is related to the forces of the fluid and vice versa. Therefore, there is a need to account for the deformation of the solid by coupling the equations from fluid mechanics and structural mechanics, resulting in fluid-structure interaction problems.

Mathematical modeling and numerical simulations in the fields of medicine and biology have been increasingly important as they enable a more successful treatment using non-invasive methods. For the arterial blood flow field, it enables more quantitative analysis of clinical studies with patient-specific data. As a consequence, scientists can gain more insight into the inherent mechanisms and improve their diagnosis techniques. Therefore, it is currently playing a vital role in advancing the understanding of pathologies in the CS such as aneurysms and stenosis.

Nonetheless, to reach this level in the study of the cardiovascular system, a great understanding of fluid mechanics, numerical methods and the cardiovascular physiology is needed. The present work starts with the study on how to solve fluid dynamics problems using the finite element method as a numerical discretization. After the solutions of fluid problems have been tested and validated, the fluid equations were coupled with solid equations using the CMM-FSI to solve blood flow problems in deformable arteries. Those simulations counted on physiological parameters provided by literature.

## 1.2 OBJECTIVE

The main objective of this work is to perform computational simulations for blood flow in deformable arteries, using idealized geometries constructed upon physiological and realistic parameters provided by literature. Those results will be compared with a fixed wall approximation. From this, the specific objectives are:

- Study of finite element method and FEniCS library to solve fluid problems;
- Compare different numerical methods for solving the Navier-Stokes equations with benchmark problems;
- Compare the numerical results from CMM-FSI with theoretical data and a rigid wall model;
- Perform blood flow simulations in deformable arteries with different shapes using CMM-FSI.

### 1.3 STRUCTURE

In this chapter, a brief introduction to what has been done in computational physiology in the blood flow area is described. Moreover, the motivation and objectives of this work are discussed.

The target of Chapter 2 is the cardiovascular system physiology. Thus, a summarized introduction will be given about some general aspects of the blood flow in arteries, its characteristics and the physical principles of the circulation.

Chapter 3 presents the mathematical background for modeling fluid and solid mechanics problems. The FSI will be presented. In this chapter, the governing equations and its constitutive relationships using partial differential equations (PDEs) or also named strong form are discussed.

In Chapter 4, the equivalent variational formulation (weak form) for the equations discussed in the previous chapter and the numerical approach by the finite element method are presented. Furthermore, a usual strategy for solving the Navier-Stokes equations and the fluid-structure with the CMM-FSI problem will be discussed.

In Chapter 5, the finite element library, FEniCS, is presented. The stabilizations for the standard Galerkin method for solving Navier-Stokes equations are compared. The benchmark problems are tested using CPU time and error for different levels of mesh refinement is made as a way to evaluate and explore the FEniCS library and the function of each stabilization term.

Chapter 6 presents the main idea of this study that is the numerical investigation of FSI problems. The CMM-FSI is tested over the Poiseuille theory. A comparison between a rigid wall and deformable wall models are made. Finally, CMM-FSI is applied to a study of pathology.

In Chapter 7, the conclusions of this work are made and suggestions for future works are presented.

## 2 ARTERIAL CIRCULATION

The focus of this work is to perform numerical simulations of blood flow in the arterial vessel of the CS. Therefore, this chapter presents a brief overview of the CS, circulation and the blood itself.

### 2.1 CARDIOVASCULAR SYSTEM

The CS is a closed circuit with the main function of transport oxygen and nutrients to all tissues and organs of the body [16]. The systemic circulation, the focus of this work, is composed of arteries, that carry the oxygenated blood ejected by the left ventricle to the living tissues. The blood first enters the aorta (the largest artery, with 2.5 *cm* of diameter) and then flows through a network, decreasing its size and reaching all the regions of the body [1].

#### 2.1.1 Blood pressure and arterial stiffness

The blood pressure is the pressure exerted by the circulating blood upon the walls of blood vessels in the whole body, where the pressure waves are formed mainly due to the pumping action of the heart. Therefore, the simulation studies of pressure waves in the human system have a significant role in the diagnosis of the diseased area of the human body [16]. The blood pressure assumes the same range of values (70-130 *mmHg*) along the entire systemic arterial tree.

In accord with O'Rourke *et al.* [2], it has been demonstrated that higher systolic blood pressure is associated with higher cardiovascular risk. For each level of systolic blood pressure, the risk is higher when pulse pressure, i.e., the difference between systolic and diastolic blood pressure, is larger. Pulse pressure is directly related to arterial stiffness.

Pulse pressure and arterial stiffness determine, together with the geometrical characteristics of the vessel, the mechanical stress within the arterial wall [42]. Arterial stiffness is involved in 3 out of the 4 major stress factors acting on the arterial wall: peak stress (systolic blood pressure), change in stress (pulse pressure), the velocity of the change in stress and stress frequency (heart rate).

Further, arterial stiffness and distensibility are difficult to measure directly in the human arterial system. Normally, stiffness is low in the proximal thoracic aorta and stiffness is greater in the abdominal aorta and peripheral arteries [2]. Besides, pressure pulsation is not the same in all arteries and diameter change is small, and hard to measure accurately. Distensibility and stiffness are useful and necessary concepts and had been used in the past to characterize properties of the arterial tree.

### 2.1.2 Blood pulse wave and wave reflection phenomena

The flow waveform plays a vital role in the study of blood flow through arteries. According to [1], the waveform of the flow rate is a function of time and characterized by different peak values. In particular, the flow rate from  $200 \text{ cm}^3/\text{s}$  in the aorta,  $80 \text{ cm}^3/\text{s}$  in the abdominal aorta,  $15 \text{ cm}^3/\text{s}$  in the carotids and  $1 \text{ cm}^3/\text{s}$  in coronaries. Those different characteristics of flow rate in the arteries result in a different value of the Reynolds number ( $Re$ ), which is explained in details in Section 3.1. Figure 1 illustrates the main arteries of the systemic circulation.

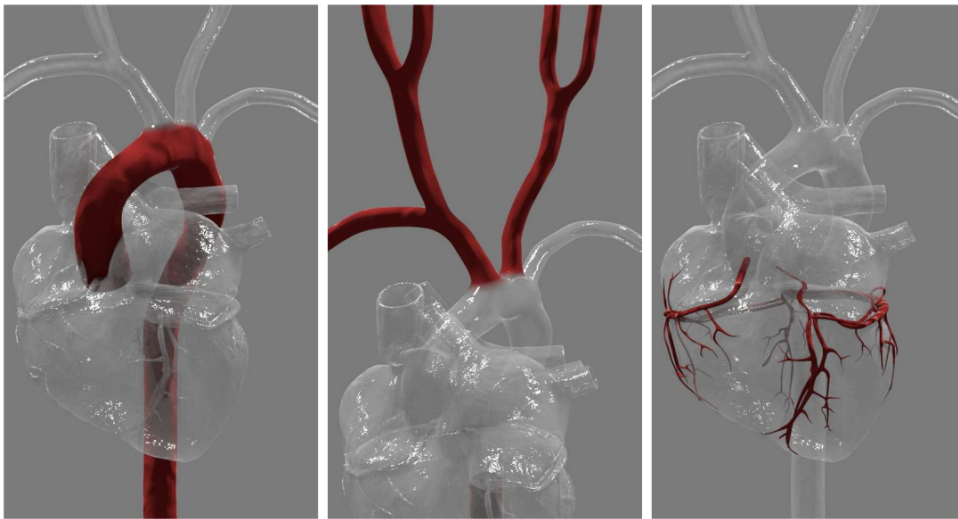


Figure 1 – Visualization of the aorta (left), carotids (middle) and coronaries (right). Taken from [1].

The pulse wave velocity ( $PWV$ ) is the speed of the pulse wave generated by the heart, along the arterial tree. It is determined by properties of the arterial wall and of blood within. It is determined by the stiffness of the segments of arterial tree traversed by the pulse according to the Moens-Korteweg equation [2]:

$$PWV = \sqrt{\frac{E/\zeta}{\mu D}}, \quad (2.1)$$

where  $E$  is the stiffness of the arterial wall as Young's modulus,  $\zeta$  is wall thickness,  $\mu$  is kinematic viscosity of blood, and  $D$  is the vessel diameter.

Therefore, since flow waveform plays a vital role in the cardiovascular system, the wave velocity may be a metric used to evaluate pathologies. This velocity ranges from about  $500 \text{ cm}/\text{s}$  in the aorta to  $1200 \text{ cm}/\text{s}$  in coronaries [1]. The presence of bifurcations or high resistance regions (such as the microvasculature) produces wave reflections propagating backward to the heart.

The wave reflection phenomena can be visualized in Figure 2 and it is understood by considering the difference between pressure and flow waves in the ascending aorta. The

flow wave from the heart shows a single spurt, whereafter flow falls to zero at the incisura, and stays at zero throughout diastole. In contrast, the pressure wave shows two localized peaks, the first corresponding to the peak of the flow and the second to the summation of reflection from multiple sites, principally in the trunk and lower body.

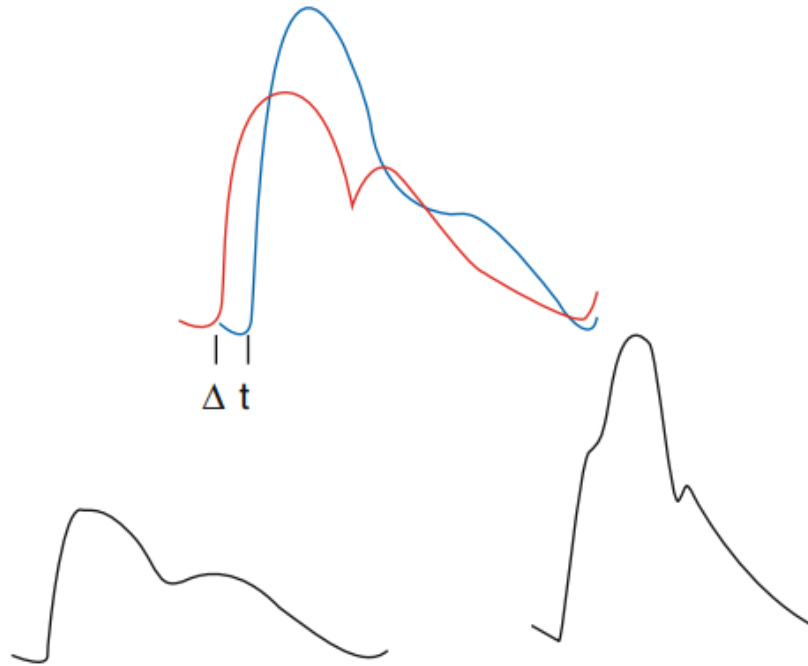


Figure 2 – The time delay ( $\Delta t$ ) due the pressure wave travelling from the ascending aorta (red) to the femoral artery (blue). Taken from [2].

### 2.1.3 Large Vessels

In large vessels, which include large cavities such as the ventricles and atria inside the myocardium as well as the large arteries and veins, the blood essentially behaves as a Newtonian fluid. The interaction between the blood cells with their pronounced elastic properties is also minimal at this scale. However, in some pathological situations, non-Newtonian effects are important even in the big cavities and large vessels and therefore they should be considered in the flow model [43].

Since the flow conditions and the impact of the blood rheology are highly dependent on the shape and size of the blood vessels, it is possible to divide the systemic circulation in three most important systems, which may be modeled and analyzed differently. The first one is the large blood vessels, which mainly apply to arteries and veins. This subsystem is followed by the small blood vessels, which broadly include capillaries and possibly arterioles. For the last, there is the porous tissue, such as the myocardium and muscles in general.

Vessel wall displacements are quite large, reaching up the value of 10% of the lumen

diameter. This is possible thanks to the structure of the vessel walls: their total thickness is about 10% of the lumen diameter and is composed of three layers, the intima, the media, and the adventitia. This gives a mutual exchange of energy between blood and vessel walls. The accumulated elastic potential energy under the forces exerted by the blood pressure, which is then transferred to the blood as kinetic energy [26, 44, 45]. Figure 3 shows schematically the composition of a blood vessel wall.

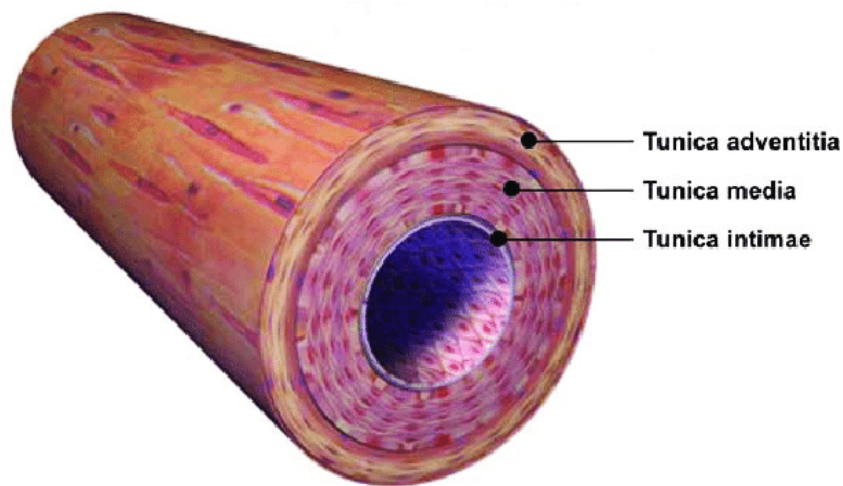


Figure 3 – The blood vessel simplified anatomy. Modified from [3].

#### 2.1.4 Carotid artery

The carotid arteries are major blood vessels in the neck that supply blood to the brain, neck, and face. As can be seen in Figure 4, there are two carotid arteries, one on the right and one on the left. In the neck, each common carotid artery branches into two divisions: the internal carotid artery supplies blood to the brain and the external carotid artery supplies blood to the face and neck. The study in blood flow in this artery is important for the prevention of stroke in patients with symptomatic or asymptomatic carotid artery stenosis.

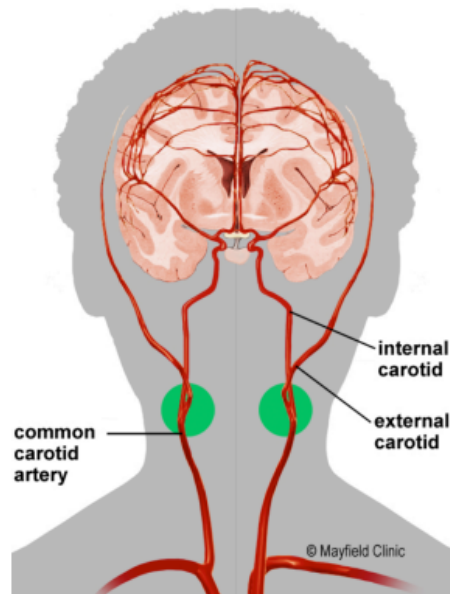


Figure 4 – The common carotid artery divides into the internal and external carotid arteries. Source: [4].

## 2.2 BLOOD

Blood is a heterogeneous multi-phase mixture of solid corpuscles suspended in liquid plasma. It is composed of plasma (about 55% of its total volume) which consists of water (about 92% of plasma volume), proteins and ions. The remaining part of blood corresponds to the blood cells, whose 97% of the volume is occupied by *erythrocytes* (red blood cells) that carry the oxygen in oxygenated blood. The other cells are *leukocytes* (white blood cells) and platelets. The diameter of blood cells is approximately  $10^{-3}cm$ , whereas that of the smallest arteries/veins is about  $10^{-1}cm$ . This is the reason why blood in the systemic and pulmonary circulations is often considered as Newtonian, i.e., characterized by a linear relationship between internal forces and velocity gradients [45, 46]. Figure 5 illustrates the blood composition.

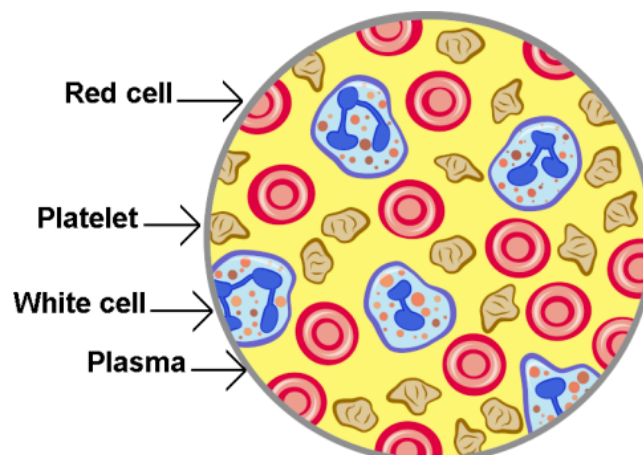


Figure 5 – Simplified illustration of the main blood composition. Source: [5].

### 3 MATHEMATICAL MODELING

For the study of blood flow problems, the equations of fluid flow and its constitutive relations must be well understood. In more realistic studies, equations for the fluid flow must be coupled with equations of elasticity, or in the optimal case, hyperelasticity or poroelasticity. The underlying concepts of these kinds of problems were developed initially somewhat independently within petroleum engineering, geomechanics, and hydrology. In this chapter, at first, an overview of solid and fluid mechanics will be presented separately. However, as this work is focused on the blood flow through the arterial system, the thin-walled solid and coupling strategy for FSI are discussed.

For this chapter, some mathematical notation will be provide. The time derivative is expressed by  $\dot{x} = \frac{dx}{dt}$ . Bold functions ( $\mathbf{x}$ ) means a vector and with a bar  $\bar{\mathbf{x}}$  is a tensor. The italic is used for scalars  $x$ .

#### 3.1 FLUID MECHANICS

Fluid mechanics is the physics and mathematical study concerned with liquids, gases, and plasmas by the laws that govern their behavior. These bases are fundamental to many applications in modeling and engineering [6]. The first aspect of this area is the definition of a fluid: “*A fluid is a substance that deforms continuously under the application of a shear (tangential) stress no matter how small the shear stress may be*” [47].

One of the most fundamental concepts in fluid mechanics problems is the Reynolds number ( $Re$ ).  $Re$  is a dimensionless number used to determine the flow regime as laminar ( $Re < 2100$ ) or turbulent ( $Re > 4100$ ). This number represents the quotient of inertia forces ( $\mathbf{u}\rho$ ) by viscosity forces ( $\frac{\mu}{D}$ ) and plays a fundamental role when solving fluid problems numerically [48]. The  $Re$  expression is given by:

$$Re = \frac{\rho \mathbf{u} D}{\mu}, \quad (3.1)$$

where for this work,  $\rho$  is the blood density,  $\mathbf{u}$  is the blood mean velocity.

It is also important to define the fluid as a continuum. The underlying molecular nature of fluids is one in which the mass is not continuously distributed in space, see Figure 6, but is concentrated in molecules that are separated by relatively large regions of the space. The concept of a continuum is the basis of classical fluid mechanics. The continuum assumption is valid in treating the behavior of fluids under normal conditions as for blood flow in the cardiovascular system [6]. Figure 6a shows how the mass is distributed in a volume, and Figure 6b shows how it may depend on the size and position of the infinitesimal volume  $\delta V$  chosen.

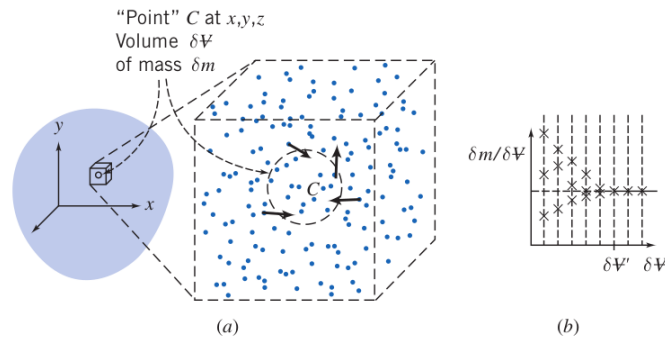


Figure 6 – Molecular distribution in a fluid particle. Source: [6].

Following the fluid mechanics discussion, the most fundamental equations in fluid flow are the conservation laws. Those equations are based on classical mechanics and state conservation of mass, momentum and energy. In the literature, these are often referred to as balance equations.

### 3.1.1 Mass conservation

In classical physics, mass can neither be destroyed nor created [49]. Therefore, mass can change over time only by flow in and out of a boundary. The principle of conservation of mass states that *the total mass of any part  $\partial\mathbf{B}$  of the body  $\mathbf{B}$  does not change in any motion*. The equation, also known as the continuity equation, that expresses local conservation of mass at any point in a continuous medium is given by:

$$\dot{\rho} + \nabla \cdot (\rho \mathbf{u}) = 0. \quad (3.2)$$

### 3.1.2 Momentum balance

Besides mass conservation a fluid also obeys conservation of momentum (i.e., Newton's second law). Recall that the momentum of a particle with mass  $m$  and velocity  $\mathbf{u}$  is defined as the product  $\mathbf{p} = m\mathbf{u}$ , and that Newton's second law says that the rate of change of momentum is equals the total external forces  $\mathbf{f}$  acting on the particle, that is,  $\dot{\mathbf{p}} = \mathbf{f}$ . The momentum  $d\mathbf{p}$  of a small volume of fluid  $dV$  is given by  $d\mathbf{p} = \rho \mathbf{u} dV$ , so taking into consideration the fact that momentum can be transported in and out of the boundary  $\partial\Omega$  of the domain  $\Omega$ , the equation for momentum balance is:

$$\rho \dot{\mathbf{u}} + \rho (\mathbf{u} \cdot \nabla) \mathbf{u} = \nabla \cdot \bar{\sigma} + \mathbf{f}, \quad (3.3)$$

where  $\bar{\sigma}$  is the total fluid stress tensor.

### 3.1.3 Constitutive relationship for blood flow problems

While blood is indeed a complex fluid, as discussed in Section 2.2, the corresponding deviations from the simple Newtonian behavior are usable as long as the flow cross sections are sufficiently large [50], as is the case in this work. As a consequence, blood is considered as a Newtonian fluid and many other studies have employed the same Newtonian approximation (e.g., [51, 52]).

- **Laminar flow:** As discussed in Section 3.1, the hypothesis of laminar flow depends on the  $Re$ . For this work, all simulations presents laminar profile, with  $Re < 2000$ .
- **Incompressible flow:** Incompressible means no change in specific mass over time  $\dot{\rho} = 0$ . In this case, mass conservation equation (3.2) reduces to  $\nabla \cdot (\mathbf{u}) = 0$ .
- **Isotropic:** The fluid is isotropic, i.e., its properties are independent of direction, and therefore the deformation law is independent of the coordinate axes in which it is expressed.

### 3.1.4 Newtonian fluid

The assumption of a Newtonian fluid requires the viscous stresses to be linear functions of the components of the strain-rate tensor, denoted by  $\gamma$ . The assumptions of Newtonian Fluid were first made by Stokes in 1845. The stresses acting in a fluid particle are of two types: internal pressure ( $\bar{\sigma}_1$ ) and viscous stresses ( $\bar{\sigma}_2$ ). The internal pressure stress ( $\bar{\sigma}_1$ ) is given by:

$$\bar{\sigma}_1 = -p\bar{I} , \quad (3.4)$$

where  $I$  is  $d \times d$  identity tensor and  $p$  is the pressure acting in the fluid particle. The viscous stress is given by:

$$\bar{\sigma}_2 = \mu(\nabla\mathbf{u} + \nabla\mathbf{u}^T) , \quad (3.5)$$

where  $\mu$  is the fluid viscosity. Viscosity is a measure of the resistance of a fluid deformed by stresses. It is commonly perceived as the thickness of the fluid. Thus, the stress tensor of a Newtonian fluid is given by:

$$\bar{\sigma} = -pI + \mu(\nabla\mathbf{u} + \nabla\mathbf{u}^T) . \quad (3.6)$$

In this work, the blood will be considered a Newtonian fluid, but Non-Newtonian fluids have been studied by several authors (e.g., [53, 54, 55]). Several factors determine the viscosity of blood, such as the viscosity of plasma, hematocrit level and blood cell distribution. While plasma is essentially a Newtonian fluid, the blood as whole behaves as a non-Newtonian fluid where red blood cells concentration is important. This usually

happens in small vessels because of the low difference between its diameter and the red blood cells size.

### 3.1.5 The Navier-Stokes equations

The famous Navier-Stokes equations describe the motion of viscous fluid particles. Those equations are based on the continuum concepts of mass and momentum conservation and the constitutive relationship of the fluid. Inserting all the concepts described above, the incompressible NSE for a Newtonian fluid are given by [34]:

$$\left\{ \begin{array}{l} \rho \dot{\mathbf{u}} + \rho(\mathbf{u} \cdot \nabla) \mathbf{u} = \nabla \cdot \bar{\boldsymbol{\sigma}} + \mathbf{f} \text{ in } \Omega \times (0, T), \\ \nabla \cdot \mathbf{u} = 0 \text{ in } \Omega \times (0, T), \\ \bar{\boldsymbol{\sigma}}(\mathbf{u}, p) = 2\mu \bar{\boldsymbol{\epsilon}}(\mathbf{u}) - p \bar{\mathbf{I}}, \\ \bar{\boldsymbol{\epsilon}}(\mathbf{u}) = \frac{1}{2}(\nabla \mathbf{u} + \nabla \mathbf{u}^T), \\ \mathbf{u} = \mathbf{g} \text{ on } \Gamma_g \times (0, T), \\ \mathbf{t}_n = \bar{\boldsymbol{\sigma}}(\mathbf{u}, p) \mathbf{n} = \mathbf{h} \text{ on } \Gamma_h \times (0, T), \\ \mathbf{u}(\mathbf{x}, 0) = \mathbf{u}^0(\mathbf{x}) \text{ in } \Omega^0 \times (0, T), \\ p(\mathbf{x}, 0) = p^0(\mathbf{x}) \text{ in } \Omega^0 \times (0, T), \end{array} \right. \quad (3.7)$$

where  $\Omega$  is the problem domain,  $\Gamma_g$  are the Dirichlet boundaries,  $\Gamma_h$  are the Neumann boundaries and  $\Omega^0$  is the initial condition of domain,  $\bar{\mathbf{I}}$  is the identity tensor,  $\mathbf{n}$  is the normal vector,  $\mathbf{g}$  is the prescribed Dirichlet condition,  $\mathbf{h}$  is the prescribed Neumann condition and finally,  $\mathbf{u}^0$  and  $p^0$  are the initial velocity and pressure respectively.

The NSE are written in divergence form, where the Cauchy stress tensor  $\bar{\boldsymbol{\sigma}}$  is explicitly included in the momentum equation and contributes to the momentum through its divergence. Those equations are coupled and non-linear, and can generally not be solved analytically. It also needs a defined initial and boundary conditions. Hence, numerical solutions are a necessity to obtain useful solutions to real-life problems.

## 3.2 SOLID MECHANICS: LINEAR ELASTICITY

Solid mechanics is the mathematical study of how solid objects deform and become internally stressed due to prescribed loading conditions. In this work, the simplification of linear elasticity will be used for modeling the wall of the vessel. In practical applications, the use of linear elasticity is limited, or more generally, the linear behavior often precludes in obtaining a non-accurate assessment of the solution because of the presence of “nonlinear” effects and/or because of the geometry has “thin” dimension in at least one direction.

Linear elasticity is an approximation used for solids subjected to small deformations, which is fitful for the arterial system for a physiological range of pressures. Following the

continuum idea, for the solid, also the change in momentum must be equal the applied forces to the system as well as body forces. So linear elasticity described in [56] is given by:

$$\begin{cases} \rho^s \ddot{\mathbf{v}} = \nabla \cdot \bar{\boldsymbol{\sigma}}^s + \mathbf{F}_v & \text{in } \Omega^s \times (0, T), \\ \mathbf{v} = \mathbf{g}^s & \text{on } \Gamma_g^s \times (0, T), \\ \mathbf{t}_n = \bar{\boldsymbol{\sigma}}^s \cdot \mathbf{n} = \mathbf{h}^s & \text{on } \Gamma_h^s \times (0, T) \\ \mathbf{v}(\mathbf{x}, 0) = \mathbf{v}^0 & \text{in } \Omega^s \\ \dot{\mathbf{v}}(\mathbf{x}, 0) = \dot{\mathbf{v}}^0 & \text{in } \Omega^s \end{cases} \quad (3.8)$$

where  $\mathbf{v}$  is the displacement vector,  $\rho^s$  is the wall density,  $\bar{\boldsymbol{\sigma}}^s$  is the wall stress tensor,  $\mathbf{F}_v$  is the prescribed body force per unit volume,  $\mathbf{v}^0$  and  $\dot{\mathbf{v}}^0$  are the given initial conditions for displacement and velocity, respectively. Furthermore,  $\Gamma_g^s$  and  $\Gamma_h^s$  represent the parts of the boundary of  $\Omega^s$  where the essential  $\mathbf{g}^s$  and natural  $\mathbf{h}^s$  boundary conditions are prescribed, respectively.

### 3.2.1 Constitutive relationship for blood vessel mechanics

We start by recalling the constitutive equation for a linear, elastic material. For elastic materials, Hooke's law represents the material behavior and relates the unknown stresses and strains. The general equation for this law using the inner product of two tensors is [7]:

$$\bar{\boldsymbol{\sigma}}^s = \bar{C} : \bar{\boldsymbol{\epsilon}}, \quad (3.9)$$

where  $\bar{C}$  is a fourth-order tensor of material stiffness and  $\bar{\boldsymbol{\epsilon}}$  is the infinitesimal strain tensor given by:

$$\bar{\boldsymbol{\epsilon}} = \frac{1}{2} \left( \nabla \mathbf{v} + (\nabla \mathbf{v})^T \right). \quad (3.10)$$

### 3.2.2 Thin-walled structure

In this work, a thin-walled structure will be assumed for the solid domain (walls), so this section will provide a suitable expression for the solid stress tensor  $\bar{\boldsymbol{\sigma}}^s(\mathbf{v})$ , particularized for a membrane-like behavior. This idea is graphically represented in Figure 7. The consideration of a thin-walled structure (membrane) model for the vessel wall nodes will enable a strong coupling of degrees-of-freedom of the fluid and solid domains and will result in an expression for the unknown integral traction (see Section 4.3). This approximation is justified by experimental evidence showing that the vessel wall constitutive behavior can be reasonably assumed as linear within the physiological range of pressures [57].

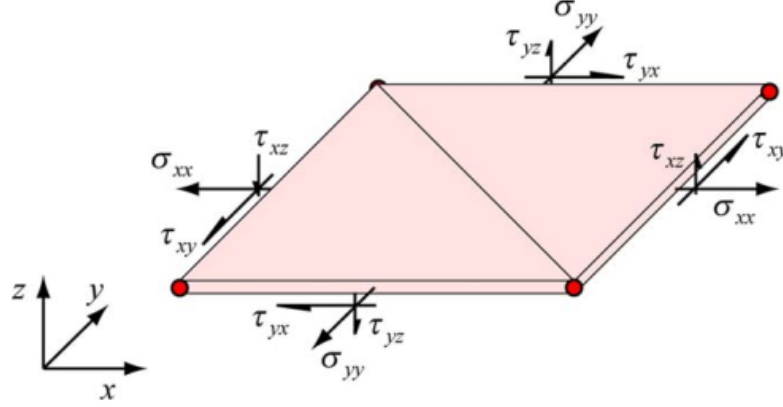


Figure 7 – Stress of a typical membrane patch with transverse shear. Taken from [7].

The use of a thin membrane approximation can neglect variations across the thickness and using symmetries, and it is possible to work with a reduced vector form of this tensor given by [7]:

$$\bar{\sigma}^{s,l} = \begin{bmatrix} \sigma_{xx}^l \\ \sigma_{yy}^l \\ 0 \\ \tau_{xy}^l \\ \tau_{xz}^l \\ \tau_{yz}^l \end{bmatrix}, \quad \bar{\epsilon}^l = \begin{bmatrix} \frac{\partial u^l}{\partial x^l} \\ \frac{\partial v^l}{\partial y^l} \\ 0 \\ \frac{\partial u^l}{\partial y^l} + \frac{\partial v^l}{\partial x^l} \\ \frac{\partial w^l}{\partial x^l} \\ \frac{\partial w^l}{\partial y^l} \end{bmatrix}, \quad (3.11)$$

where  $u^l, v^l$  and  $w^l$  are the three components of the displacement vector  $\mathbf{u}^l$  and  $x^l, y^l$  are the local nodal coordinates. Now, it is possible to define a second-order tensor of material constants  $\bar{D}$  which relates the following local stress and strain vectors for a plane stress state of an incompressible, isotropic solid augmented by the transverse shear stresses  $\tau_{xy}^l$  and  $\tau_{yz}^l$ . This tensor can be written as follows [7]:

$$\bar{D} = \frac{E}{(1-\nu^2)} \begin{bmatrix} 1 & \nu & 0 & 0 & 0 \\ \nu & 1 & 0 & 0 & 0 \\ 0 & 0 & 0.5(1-\nu) & 0 & 0 \\ 0 & 0 & 0 & 0.5k(1-\nu) & 0 \\ 0 & 0 & 0 & 0 & 0.5k(1-\nu) \end{bmatrix} \quad (3.12)$$

where  $\nu$  is the Poisson's ratio coefficient and the parameter  $k$  accounts for a parabolic variation of transverse shear stress through the membrane. For a solid, homogeneous plate this parameter takes the value of 5/6 [58, 59].

Therefore, the equation (3.9) is modified for this work and the solid stress tensor becomes [7]:

$$\bar{\sigma}^s = \bar{D} : \bar{\epsilon}. \quad (3.13)$$

### 3.2.3 Initial, boundary and interface conditions

Before the equations can be solved, appropriate boundary and initial conditions need to be imposed to yield a unique velocity-pressure pair. For a specific fluid occupying a domain, the treatment of initial and boundary conditions is what distinguishes different flow patterns as the governing equations inside the domain stay the same. A fluid generally moves around between solid boundaries,  $\Omega^s$ , and boundaries known as traction boundaries  $\Gamma_s$ .

The initial conditions  $\mathbf{u}^0$  and  $p^0$ , if not specified in the problem, is  $\mathbf{u}^0 = \mathbf{0}$  and  $p^0 = 0$ . Further, when applying the CMM-FSI, the initial conditions are the pressure and velocity from the rigid case, i.e:  $\mathbf{u}_d^0 = \mathbf{u}_r^n$  and  $p_d^0 = p_r^n$ , where  $d$  and  $r$  means deformable and rigid respectively. The initial displacement  $\mathbf{v}^0$  is based on the CMM-FSI and it is the hydrostatic pressure at the rigid wall.

For this work, on boundary  $\Gamma_s$ , e.g, the interface between a fluid and a solid wall, the fluid velocity ( $\mathbf{u}$ ) must equal the wall velocity( $\dot{\mathbf{v}}$ ) in all directions. A special case for the rigid wall assumption is the boundary condition to be  $\mathbf{u} = \dot{\mathbf{v}} = \mathbf{0}$  on  $\Gamma_s$ , often named no-slip boundary condition.

The domains and boundaries are illustrated in Figure 8. The symbols  $\Gamma_g$  and  $\Gamma_h$  represent the inlet and outlet boundaries, respectively.  $\Gamma_s$  is the interface between the solid and fluid domains,  $\partial\Gamma$  represents all boundaries left of the fluid domain,  $\zeta$  is the wall thickness and  $\Omega$  and  $\Omega^s$  represent the fluid and solid domains, illustrated by blue and red, respectively.

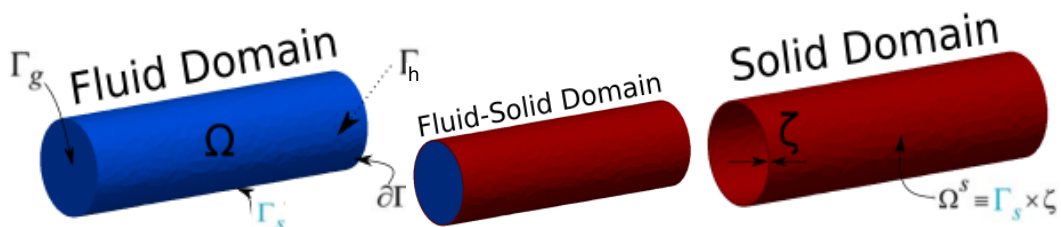


Figure 8 – Schematic representation of the fluid and solid domains and their boundaries. Adapted from [7].

### 3.3 FLUID STRUCTURE INTERACTION

It is described in [16] how arterial wall mechanics plays a vital role in a hemodynamic problem. As discussed in Section 2.1, the mechanical interaction between blood and the arterial wall is the fundamental responsibility for the propagation of pressure waves from the heart to the whole body. This interaction is an important factor that helps to regulate blood pressure in the circulation system. An efficient and accurate numerical simulation of this mechanism have an important role in the hemodynamics study for preparing medical devices and medical treatment.

One of the better-known methods for including wall deformability is the ALE formulation for FSI problems [22, 23]. However, ALE formulations are computationally expensive when considering large models of the vasculature and not very robust since they need, to update constantly the geometry of the fluid and structural elements.

This work aims to use the CMM-FSI described in [7], due to its simple construction implementation, with a strong coupling of degrees-of-freedom of the fluid and the solid domains, coupling the vessel wall deformation at the variational level as a boundary condition for the fluid domain. This formulation starts from a conventional stabilized finite element the formulation for the NSE in a rigid domain and modifies it in such a way that the deformation of the wall domain surrounding the fluid is taken into account. Therefore, this coupling between fluid and solid equations is done in a variational level. In this method, the acceleration term  $\ddot{\mathbf{v}}$  will be written as the time derivative of the velocity ( $\mathbf{u}$ ) rather than as the second time derivative of the displacement field ( $\mathbf{v}$ ) since the goal is to express the vessel wall equations in terms of the unknown fluid parameters.

To use the CMM-FSI we will solve the NSE with a Neumann BC of traction in the Fluid-Solid interface. So first, we define the inflow and outflow conditions and solve only the NSE with no-slip BC in the interface  $\Gamma_s$  to find  $\mathbf{u}_r$  and  $p_r$ . Thus, in equation 3.18 we have:

$$\mathbf{u} = \mathbf{0} \quad \text{on } \Gamma_s \times (0, T), \quad (3.14)$$

$$\mathbf{t}_n = \mathbf{0} \quad \text{on } \Gamma_s h \times (0, T), \quad (3.15)$$

$$\mathbf{u}(\mathbf{x}, 0) = \mathbf{0} \quad \text{in } \Omega^0 \times (0, T), \quad (3.16)$$

$$p = 0 \quad \text{in } \Omega^0 \times (0, T). \quad (3.17)$$

Next, the no-slip BC is removed and replaced by the traction related to the solid equations. However, this is done in a variational level and explained in Section 4.3. Therefore, the velocity  $\mathbf{u}_r$  and pressure  $p_r$  are the initial conditions for the coupled

problem. So the strong form of the CMM-FSI used in this work can be written by:

$$\left\{ \begin{array}{l} \rho \dot{\mathbf{u}} + \rho(\mathbf{u} \cdot \nabla) \mathbf{u} = \nabla \cdot \bar{\boldsymbol{\sigma}} + \mathbf{f} \text{ in } \Omega \times (0, T), \\ \nabla \cdot \mathbf{u} = 0 \text{ in } \Omega \times (0, T), \\ \dot{\mathbf{u}} = \ddot{\mathbf{v}}, \\ \bar{\boldsymbol{\sigma}}(\mathbf{u}, p) = 2\mu \bar{\boldsymbol{\epsilon}}(\mathbf{u}) - p \bar{\mathbf{I}}, \\ \bar{\boldsymbol{\epsilon}}(\mathbf{u}) = \frac{1}{2}(\nabla \mathbf{u} + \nabla \mathbf{u}^T), \\ \bar{\boldsymbol{\sigma}}^s = \bar{\mathbf{D}} : \bar{\boldsymbol{\epsilon}}, \\ \mathbf{u} = \mathbf{g} \text{ on } \Gamma_g \times (0, T), \\ p = P \text{ on } \Gamma_h \times (0, T), \\ \mathbf{t}_n = \bar{\boldsymbol{\sigma}}^s \cdot \mathbf{n} = \mathbf{h}^s \text{ on } \Gamma_s \times (0, T), \\ \mathbf{u}(\mathbf{x}, 0) = \mathbf{u}_r \text{ in } \Omega^0 \times (0, T), \\ p(\mathbf{x}, 0) = p_r \text{ in } \Omega^0 \times (0, T), \\ \mathbf{v}(\mathbf{x}, 0) = \mathbf{v}^0(\mathbf{x}) \text{ in } \Omega^0 \times (0, T), \\ \dot{\mathbf{v}}(\mathbf{x}, 0) = \mathbf{u}(\mathbf{x}) \text{ on } \Gamma_s \times (0, T). \end{array} \right. \quad (3.18)$$

where  $\mathbf{g}$  and  $P$  are the prescribed flow and pressure functions at inlet and outlet respectively, and  $\mathbf{v}^0$  is the initial displacement, discussed at Section 4.4.1.

## 4 NUMERICAL METHODS

This chapter discusses the variational formulation (weak form) for the partial equations discussed in chapter 3. The FEM is presented as a way to discretize the continuum variational approach. The Galerkin method and the stabilizations SUPG, PSPG and LSIC are presented to solve fluid dynamics problems. The FSI is presented combining the solid mechanics with the stabilized Navier-Stokes equations in the variational level.

### 4.1 FINITE ELEMENT METHOD

The FEM is a popular solution strategy to solve partial differential equations [60]. Its success is due to its feasibility to a majority kind of differential equations. Furthermore, it is very flexible concerning complex geometries and it is easy to construct higher-order approximations.

This method was presented late in the 1950s in the aircraft industry and was the first design to solve solid mechanics problems. Felippa [60] presents a historical outline, showing that FEM is one of the most powerful numerical methods emerged so far. Second to Logg *et al.* [8], this method emerged as an universal method for the solution of differential equations due to its generality, elegance, and flexibility of formulation, allowing the properties of the discretization to be controlled by the choice of approximating finite element spaces. FEM is a pragmatic way to transform a PDE in a variational formulation and so on in a linear system.

The main constituents of a FEM for the solution of a boundary-value problem are given by the flow chart in Figure 9.

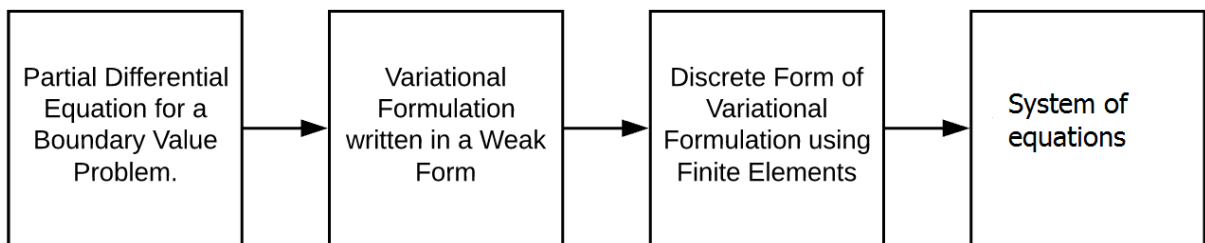


Figure 9 – Flow chart of PDE to linear/nonlinear system.

### 4.2 FLUID PROBLEM DISCRETIZATION

Equations (3.1.5) are in the strong form of the boundary value problem. This Section discusses the stabilized Galerkin formulation for the solid and fluid strong equations, in order to obtain the weak form. Stabilization methods for fluid equations are also discussed.

#### 4.2.1 Galerkin formulation

This section aims to find the weak form of the NSE. This means local approximations for velocity  $\mathbf{u}^h$  and pressure  $p^h$ , the trial functions, are introduced as well as the associated test functions  $\mathbf{w}^h$  and  $q^h$ . Note that, trial functions require that they fulfill the Dirichlet boundary condition, whereas the test functions have to be zero. For these definitions to be valid, we assume that the functions  $\mathbf{w}^h$  and  $q^h$  are all locally integrable [61].  $H^{1h}$  is the space that consists of piecewise continuous functions and it is well-known that  $H^{1h} \subset H^1$ . This yields in the following function spaces:

$$\mathcal{U}_v^h = \left\{ \mathbf{u} \mid \mathbf{u}(\cdot, t) \in H^1(\Omega)^d, t \in [0, T], \mathbf{u}|_{\mathbf{x} \in \Omega_e} \in P_k(\Omega_e)^d, \mathbf{u}(\cdot, t) = \mathbf{g} \text{ in } \Gamma_g \right\}, \quad (4.1)$$

$$\mathcal{W}_v^h = \left\{ \mathbf{w} \mid \mathbf{w}(\cdot, t) \in H^1(\Omega)^d, t \in [0, T], \mathbf{w}|_{\mathbf{x} \in \Omega_e} \in P_k(\Omega_e)^d, \mathbf{w}(\cdot, t) = \mathbf{0} \text{ in } \Gamma_g \right\}, \quad (4.2)$$

$$\mathcal{P}_p^h = \left\{ p \mid p(\cdot, t) \in H^1(\Omega), t \in [0, T], p|_{\mathbf{x} \in \Omega_e} \in P_k(\Omega_e) \right\}. \quad (4.3)$$

where  $\Omega \subset \mathcal{R}^d$  represents the closure of the spatial domain ( $\Omega \cup \Gamma$ ) in  $d = 3$  dimensions,  $k$  is the order of polynomial approximation,  $P_k(\Omega_e)$  is the local polynomial approximation space in  $\Omega_e$  and  $g$  represents an approximation to the prescribed Dirichlet boundary condition in the finite element basis [7].

With the help of these spaces, the semi-discrete Galerkin finite element formulation for the fluid, resulting in finding  $\mathbf{u} \in \mathcal{U}^h$  and  $p \in \mathcal{P}^m$ , in such way that [7]:

$$\begin{aligned} F(\mathbf{w}, q, \mathbf{u}, p) = & \int_{\Omega} \left( \mathbf{w}^h \cdot (\rho \dot{\mathbf{u}}^h + \rho \mathbf{u}^h \cdot \nabla \mathbf{u}^h - \mathbf{f}) + \nabla \mathbf{w}^h : (-p^h \bar{\mathbf{I}} + \bar{\boldsymbol{\sigma}}(\mathbf{u}^h)) \right) d\Omega \\ & + \int_{\Omega} q^h \nabla \cdot \mathbf{u}^h d\Omega + \int_{\Gamma_h^h} -\mathbf{w}^h \cdot \mathbf{h}^h d\Gamma + \int_{\Gamma_h^h} -\mathbf{w}^h \cdot \mathbf{t}^{f,h} d\Gamma = 0 \end{aligned} \quad (4.4)$$

$\forall \mathbf{w} \in \mathcal{W}^h$  and  $q \in \mathcal{P}^h$ .

The last term of the equation is determined based on the solid equations and it will be zero if do not be considered.

#### 4.2.2 Stabilizations for Galerkin Formulation

In the finite element computation of flow problems, stabilized formulations are among the most fundamental and important enabling technologies [33]. For a representative class of flows governed by the NSE, the standard Galerkin formulation using same order interpolator polynomials for velocity and pressure is unstable since they may not satisfies inf-sup condition defined by LBB [62]. In a way to overcome these numerical instabilities, we should choose polynomials whose degree of approximation for the pressure should be one

or two degrees lower than that for the velocity. Another approach that has been successfully considered in the last decades is adding stabilizing terms in the FEM formulation.

For this work, in order to make the Galerkin formulation stable using the same polynomial order for both pressure and velocity, additional stabilization terms must be added in equation (4.4). The stabilization parameter takes the form of the following equation [63]:

$$\sum_e \int_{\Omega^e} \mathcal{A}(w) \tau \mathcal{R}(\mathbf{u}, p) d\Omega, \quad (4.5)$$

where  $\mathcal{A}$  is a particular operator applied in the function space,  $\tau$  is the stabilization parameter and  $\mathcal{R}$  is the residual of momentum equation given by:

$$\mathcal{R}(\mathbf{u}, p) = \rho \dot{\mathbf{u}} + \rho(\mathbf{u} \cdot \nabla) \mathbf{u} + \nabla p - \mathbf{f}. \quad (4.6)$$

Applying these stabilizations, which are discussed below, the Galerkin method is ensured to be consistent. This means that the solution of the differential equation is also a solution to the weak form [63].

#### 4.2.2.1 Streamline-Upwind/Petrov-Galerkin

Streamline-Upwind/Petrov Galerkin (SUPG) stabilization is needed for convection dominated flow as the first approach to balance adding artificial diffusion. The SUPG stabilization uses this idea as a starting point but ensures that artificial diffusion is only added in a streamline direction. Thus excessive over diffusion is avoided. The extra term is defined as [31]:

$$\sum_e \int_{\Omega^e} (\mathbf{u} \cdot \nabla) \mathbf{w} \cdot \tau_{SUPG} \mathcal{R}(\mathbf{u}, p) d\Omega, \quad (4.7)$$

where  $\tau_{SUPG}$  is based on element-level matrices and vectors to automatically account for local mesh sizes, advection fields, and the fluid viscosity proposes [64]:

$$\tau_{SUPG} = \left( \left( \frac{1}{0.5\Delta t} \right)^2 + \left( \frac{2\mathbf{u}}{h_e} \right)^2 + 9 \left( \frac{4\mathbf{u}}{h_e^2} \right)^2 \right)^{-\frac{1}{2}}. \quad (4.8)$$

#### 4.2.2.2 Pressure-Stabilizing/Petrov-Galerkin

The second additional term adds a certain amount of compressibility to the system and allows the use of elements for pressure and velocity with equal-order interpolations

for velocity and pressure, which implies that the LBB condition is fulfilled. The PSPG term is given by [32]:

$$\sum_e \int_{\Omega^e} \tau_{PSPG} \nabla q \cdot \mathcal{R}(\mathbf{u}, p) d\Omega, \quad (4.9)$$

with  $\tau_{PSPG}$  being evaluated element based on the local mesh size  $h_e$ :

$$\tau_{PSPG} = \frac{h_e^2}{2}. \quad (4.10)$$

#### 4.2.2.3 Least-Squares on Incompressibility Constraint

To be used in conjunction with the SUPG/PSPG, Least-Squares on Incompressibility Constraint (LSIC) provides additional stability for convection dominated flows and in flow fields with sharp gradients as follows [33]:

$$\sum_e \int_{\Omega^e} \tau_{LSIC} \nabla \cdot \mathbf{w} : \nabla \cdot \mathbf{u} d\Omega, \quad (4.11)$$

where a typical choice of  $\tau_{LSIC}$  is:

$$\tau_{LSIC} = \|\mathbf{u}\| \frac{h_e}{2}. \quad (4.12)$$

Finally, the stabilized Galerkin method for solving the Navier-Stokes equations is: Find  $\mathbf{u} \in \mathcal{U}^k$  e  $p \in \mathcal{P}^k$ , in such way that:

$$\begin{aligned} F(\mathbf{w}, q, \mathbf{u}, p) &= \int_{\Omega} \left( \mathbf{w}^h \cdot (\rho \dot{\mathbf{u}}^h + \rho \mathbf{u}^h \cdot \nabla \mathbf{u}^h - f) + \nabla \mathbf{w}^h : (-p^h \bar{I} + \sigma(\mathbf{u}^h)) \right) d\Omega \\ &+ \int_{\Omega} q^h \nabla \cdot \mathbf{u}^h d\Omega + \int_{\Gamma_s^h} -\mathbf{w}^h \cdot \mathbf{h}^h d\Gamma + \int_{\Gamma_s^h} -\mathbf{w}^h \cdot \mathbf{t}^{f,h} d\Gamma + \sum_e \int_{\Omega^e} \tau_{PSPG} \nabla q \cdot \mathcal{R}(\mathbf{u}^h, p) d\Omega \\ &+ \sum_e \int_{\Omega^e} (\mathbf{u}^h \cdot \nabla) \mathbf{w}^h \cdot \tau_{SUPG} \mathcal{R}(\mathbf{u}^h, p) d\Omega + \sum_e \int_{\Omega^e} \tau_{LSIC} \nabla \cdot \mathbf{w}^h : \nabla \cdot \mathbf{u}^h d\Omega = 0, \end{aligned} \quad (4.13)$$

$\forall \mathbf{w} \in \mathcal{W}^h$  and  $q \in \mathcal{P}^h$ .

Equation (4.13) is still a semi-discrete formulation. Therefore, a discretization in time has to be specified. It is used a Backward Euler scheme  $\dot{\mathbf{u}} \approx \frac{\mathbf{u}^n - \mathbf{u}^{n-1}}{\Delta t}$ .

### 4.3 SOLID DISCRETIZATION

In order to relate the solid problem with the lateral boundary of the fluid domain,  $\Omega^s$  needs to be mapped on  $\Gamma_s$ . Assuming a thin-walled structure of thickness  $\zeta$ , integrals

defined on  $\Gamma^s$  and  $\Omega^s$  can be related with integrals on the lateral boundary of the fluid domain  $\Gamma_s$  according to the following expressions [7]:

$$\int_{\Omega^s} (\cdot) dx = \zeta \int_{\Gamma_s} (\cdot) ds, \quad (4.14)$$

$$\int_{\Gamma_h^s} (\cdot) dx = \zeta \int_{\partial\Gamma_h} (\cdot) dl. \quad (4.15)$$

The surface traction  $\mathbf{t}^f$  acting on the fluid lateral boundary due to the interaction with the solid is equal and opposite to the surface traction  $\mathbf{t}^s$  acting on the vessel wall due to the fluid, and since the wall is a thin-enough structure, the internal surface traction  $\mathbf{t}^s$  will be felt uniformly through the wall thickness as follows:

$$\mathbf{t}^f = -\mathbf{t}^s = -\mathbf{b}^s \zeta, \quad (4.16)$$

$$\mathbf{b}^s = \frac{-\mathbf{t}^f}{\zeta}. \quad (4.17)$$

Therefore, it is possible to relate the unknown integral term  $\int_{\Gamma_s} -w \cdot \mathbf{t}^f d\Gamma$  of equation (4.4) with the weak form for the vessel wall problem given by equation (4.17).

#### 4.3.1 Galerkin approximation

Since a strong coupling of the degrees-of-freedom of the fluid and solid domains is considered, the displacement, velocity and acceleration fields on the fluid-solid interface are identical. Furthermore, since the weak form of the elastodynamics equations has the same differentiability requirements on the functional spaces as the fluid weak form, we can adopt for the vessel wall problem the same type of functional spaces as in the fluid domain, given by equations (4.1) and (4.2). Considering this, the semi-discrete Galerkin finite element formulation produces the following weak form: Find  $\mathbf{u} \in \mathcal{U}^h$  such that

$$\int_{\sigma^s} \rho^s \mathbf{w} \cdot \dot{\mathbf{u}} dx + \int_{\Omega^s} \nabla \mathbf{w} : \sigma^s dx = \int_{\Omega^s} \mathbf{w} \cdot \mathbf{b}^s dx + \int_{\Gamma_h^s} \mathbf{w} \cdot \mathbf{h}^s ds, \quad (4.18)$$

for all  $\mathbf{w} \in \mathcal{W}^h$ . The acceleration term  $\ddot{\mathbf{v}}$  has been written as the time derivative of the velocity  $\dot{\mathbf{u}}$  rather than as the second time derivative of the displacement field since the goal is to express the vessel wall equations in terms of the fluid unknowns.

Now equations (4.14) and (4.15) are utilized to map the equation (4.18) into the lateral boundary of the fluid domain  $\Gamma_s$ . Considering the expression for the body force  $\mathbf{b}^s$  given by equation (4.17), the final expression of the weak form for the solid domain is:

$$-\int_{\Gamma^s} \mathbf{w} \cdot \mathbf{t}^f ds = \zeta \int_{\Omega^s} \rho^s \mathbf{w} \cdot \dot{\mathbf{u}} ds + \zeta \int_{\Omega^s} \nabla \mathbf{w} : \bar{\sigma}^s ds - \zeta \int_{\Gamma_h^s} \mathbf{w} \cdot \mathbf{h}^s dl. \quad (4.19)$$

#### 4.4 Combined formulation: CMM-FSI

The equation (4.19) provides an expression for the unknown term in the equation (4.4) as a function of the solid internal stresses and inertial forces. Combining these two equations result in the following weak Galerkin form for the CMM-FSI [7]:

$$\begin{aligned}
 F(\mathbf{w}, q, \mathbf{u}, p) &= \int_{\Omega} \left\{ \mathbf{w}^h \cdot (\rho \dot{\mathbf{u}}^h + \rho \mathbf{u}^h \cdot \nabla \mathbf{u}^h - \mathbf{f}) + \nabla \mathbf{w}^h : (-p^h \bar{I} + \tau(\mathbf{u}^h)) + q^h \nabla \cdot \mathbf{u}^h \right\} d\Omega \\
 &- \int_{\Gamma_h} \mathbf{w} \cdot h ds + \int_{\Gamma_h} q \mathbf{u}_n ds + \int_{\Gamma_g} q \mathbf{u}_n ds + \boxed{\zeta \int_{\Gamma_s} \left\{ \mathbf{w}^h \cdot (\rho \dot{\mathbf{u}}^h + \nabla \mathbf{w} : \sigma^s(\mathbf{u})) \right\} ds} \quad (4.20) \\
 &\boxed{-\zeta \int_{\partial \Gamma_h} \mathbf{w} \cdot h^s dl + \int_{\Gamma_s} q \mathbf{u}_n} = 0,
 \end{aligned}$$

where the boxed terms in equation (4.20) define the new terms added to rigid wall theory. The stabilization terms discussed in Section 4.2.2 may be added into equation (4.20) if necessary.

##### 4.4.1 Method to find the deformation

In accord with [7], the weak form given by equation (4.20) can be written as a semi-discrete system of nonlinear ordinary differential equations in time:

$$\begin{cases} \mathbf{R}(\mathbf{v}, \mathbf{u}, \dot{\mathbf{u}}, p) = 0 & \text{in } \Omega \\ \mathbf{u} = \dot{\mathbf{v}} & \text{on } \Gamma_s \end{cases} \quad (4.21)$$

where the vector  $\mathbf{R}$  represents the set of nodal nonlinear residuals defined for each point of the finite element mesh.

The displacement field  $\mathbf{v}$ , can be determined with the Newmark's formula, which relates the displacement field on  $\Gamma_s$  with the fluid velocity and acceleration. The time derivative of velocity will be approximated by backward finite differences.

$$\frac{\partial \mathbf{u}}{\partial t} = \dot{\mathbf{u}}_n = \frac{\mathbf{u} - \mathbf{u}^n}{\Delta t} \quad (4.22)$$

$$\mathbf{v}_{n+1} = \mathbf{v}_n + \dot{\mathbf{u}}_n + \frac{\Delta t^2}{2} \{(1 - 2\beta)\dot{\mathbf{u}}_n + 2\beta\dot{\mathbf{u}}_{n+1}\}, \quad (4.23)$$

where  $\beta = 1.0$  in this work, but the influence of this parameter on the linear stability is found in [58].

#### 4.5 ALGORITHM OF THE CMM-FSI

This section summarizes the main points of the CMM-FSI and how the solver is implemented.

**Result:**  $\mathbf{u}$ ,  $p$ ,  $\mathbf{v}$

define mixed continuous Lagrange space function;

define trial and test functions;

define Boundary Conditions;

define initial conditions;

define variational forms for equations (4.13) and (4.20) with what is necessary;

define equation 4.23;

**while**  $t \leq \text{final time } T$  **do**

    solve equation (4.13);

    update initial conditions  $\mathbf{u}^0$ ,  $\mathbf{v}^0$  and  $p^0$ ;

    update Boundary Conditions;

    solve equation (4.20);

    solve equation (4.23);

    update  $\mathbf{u}$ ,  $\mathbf{v}$  and  $p$ ;

**end**

**Algorithm 1:** Procedure of the CMM-FSI

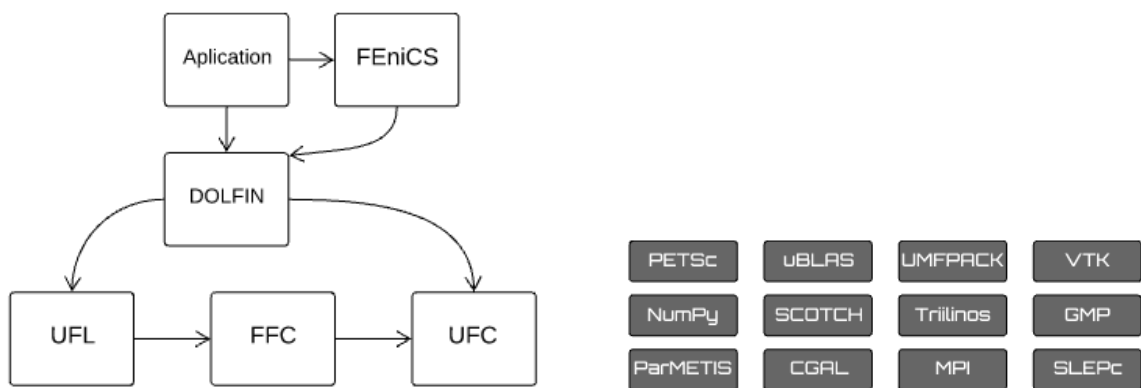
## 5 NUMERICAL INVESTIGATION FOR FLUID PROBLEMS

As discussed in Chapter 1, the first step for studying the blood flow through arteries is to handle numerically with flow problems, more specifically, to solve Navier-Stokes for incompressible flows. This chapter will use the library FEniCS to perform a comparative study for numerical simulations with stabilizations discussed in Section 4.2.2, to solve well-known flow benchmark problems. Initially, an introduction to the FEniCS library is made.

### 5.1 THE FEniCS LIBRARY

FEniCS is a program package to solve PDEs based on the FEM [8]. Its idea is to enable an automated solution of partial differential equations, this includes features for automated error control and adaptivity, a comprehensive library of finite elements, high-performance linear algebra and many more. FEniCS routines can be programmed in Python or C++. In this work, Python programming is chosen. Programming a FEniCS routine is quite straightforward since variational forms can be specified in a near-mathematical notation. After the variational form has been carried out, implementation in FEniCS is relatively simple.

The FEniCS library carries out a lot of components of free software and open-source codes, as it can be seen in Figure 10. Its main interface is DOLFIN, which provides a programming interface environment between the user and the solution for the differential equations.



(a) DOLFIN functions as the main user interface of FEniCS.

(b) External libraries.

Figure 10 – Main free software and open source codes used by FEniCS. (a) the flow chart of a FEniCS program. (b) the external libraries that FEniCS carries in. Adapted from [8].

Among the external libraries, some of them are linear algebra packages (PETSc,

uBLAS, UMFPACK, Trilinos, GMP), mesh partitioning (SCOTCH, ParMETIS, CGAL), parallel processing (MPI, SLEPc) and visualization (VTK).

Based on Figure 10, the FEniCS and applications relies on DOLFIN, which is the standard object-oriented C++ library for finite elements. Figure 11 shows the provide classes such as *Matrix*, *Vector*, *Mesh*, *FiniteElement*, *FunctionSpace* and *Function*, important structures for finite element computing. However, to solve the differential equations, users must express a finite element variational problems in the unified form language (UFL) language.

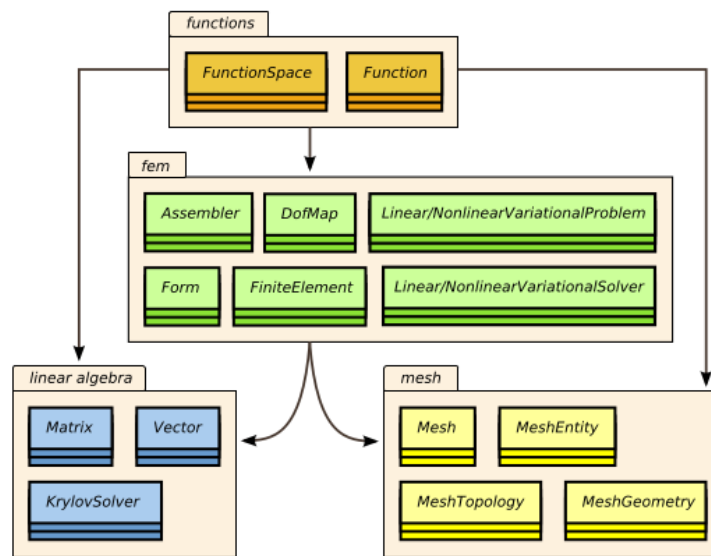


Figure 11 – Schematic overview of the most important components and classes of DOLFIN. Arrows indicate dependencies [8].

The UFL is a domain-specific language for the declaration of finite element discretization of variational forms and functionals. More precisely, the language defines a flexible user interface for defining finite element spaces and expressions for weak forms in a notation close to mathematical notation.

One of the key features of FEniCS is the automated code generation for the general and efficient solution of finite element variational problems, done by the FEniCS form compiler (FFC). In simple terms, the solution of finite element variational problems is based on two ingredients: the construction of linear or nonlinear systems of equations and the solution of those equations. So the FFC generates code for the efficient computation of the assembly of sparse matrices as well as the local-to-global mapping.

Finally, the Unified Form-assembly Code (UFC) is the central component of FEniCS. UFC is an interface between problem-specific and general-purpose components of finite element programs. In particular, the UFC interface defines the structure and signature of the code that is generated by the form compilers (FFC) for DOLFIN. To do that,

UFC applies a wide range of finite element problems (including mixed finite elements and discontinuous Galerkin methods).

## 5.2 FLUID PROBLEMS BENCHMARKS

To test the accuracy and efficiency of FEniCS, the stabilized method presented in Sections 4.2.1 and 4.2.2, a set of test problems was performed. Each test has a different measure of error, using a functional of interest or a norm of the global error. All evaluation parameter is measured in the final time, shown in Table 1.

	Reynolds Number	Final Time	Evaluation
Driven Cavity	1000	2.5	min stream function value
Pressure Driven	8	0.5	$u_i(1,0.5)$
Taylor-Green Vertex	100	0.5	Kinetic energy
Flow Around a Cylinder	1000	8.0	$p(0.15,0.2) - p(0.25,0.2)$

Table 1 – Resume of the flow problems evaluation [8].

The time step is chosen based on an approximated CFL condition  $dt = 0.2h/U$  where  $U$  is an estimate of the maximum velocity and  $h$  is the minimum cell diameter. Stable mixed finite element methods for the NSE must satisfy the LBB (or inf-sup) compatibility condition [30]. Therefore, in this work, all stabilized methods will use  $(P_1 - P_1)$  discretization with PSPG.

All simulations were performed in a single core and it was performed on a Linux platform in a simple PC with 8GB of memory and an Intel Core i5 2.5GHz. The Table 2 summarizes the solver parameters adopted in this work.

Linear Solver	GMRES
Preconditioner	ILU
Absolute Tolerance error	$10^{-10}$
Relative Tolerance error	$10^{-8}$
Non linear method	Newton
Newton Method tolerance	$10^{-6}$

Table 2 – Solver parameters for all problems.

These parameters were chosen to get an accurately solution of the linear and non-linear systems, in agreement with [8]. The generalized minimal residual method (GMRES) is chosen because of its iterative method for the numerical solution of a non-symmetric system of linear equations, which attends for all problems and it is combined with the incomplete LU factorization (ILU), standard defined with a 0 fill-level. The non-linearity is solved with the Newton method.

For each problem, the standard Galerkin method with the stabilizations SUPG,PSPG and LSIC are compared for both error and processing time for different mesh sizes.

### 5.2.1 Driven Cavity

This fluid dynamics problem is well discussed in [65] and numerically by [8] and [66]. It is a classical benchmark where a square cavity with sides of unit length. For this problem, the parameter of interest is the minimum value of the stream function ( $\psi$ ), which is dependent on the Reynolds number ( $Re$ ). Therefore, for this study, a kinematic viscosity of  $\mu = 1/1000$  is chosen for a problem with  $Re = 1000$ . No-slip boundary conditions are imposed on each edge of the square, except at the upper edge where the velocity is set to  $\mathbf{u} = (1, 0)$ . The initial velocity  $\mathbf{u}_0$  is set to zero. The resulting flow is a vortex developing in the upper right corner and then traveling towards the center of the square as the flow evolves, as it was experimental visualized by [67]. The reference value of this problem is  $\psi_{ref} = -0.0585236$  at  $T = 2.5$  [8]. This reference value is the minimum value of  $\psi$ . The flux equation is given by [68]:

$$\mathbf{u} = \nabla \times \psi = \left( \frac{\partial \psi}{\partial y} - \frac{\partial \psi}{\partial x} \right), \quad (5.1)$$

and may be solved using the Poisson equation:

$$-\nabla^2 \psi = \omega, \quad (5.2)$$

where  $\omega$  is the vorticity, defined as:

$$\omega = \nabla \times \mathbf{u} = \frac{\partial u_j}{\partial x} - \frac{\partial u_i}{\partial y}. \quad (5.3)$$

Figure 12 shows the numerical results of velocity and streamlines at time  $t = 2.5$ .

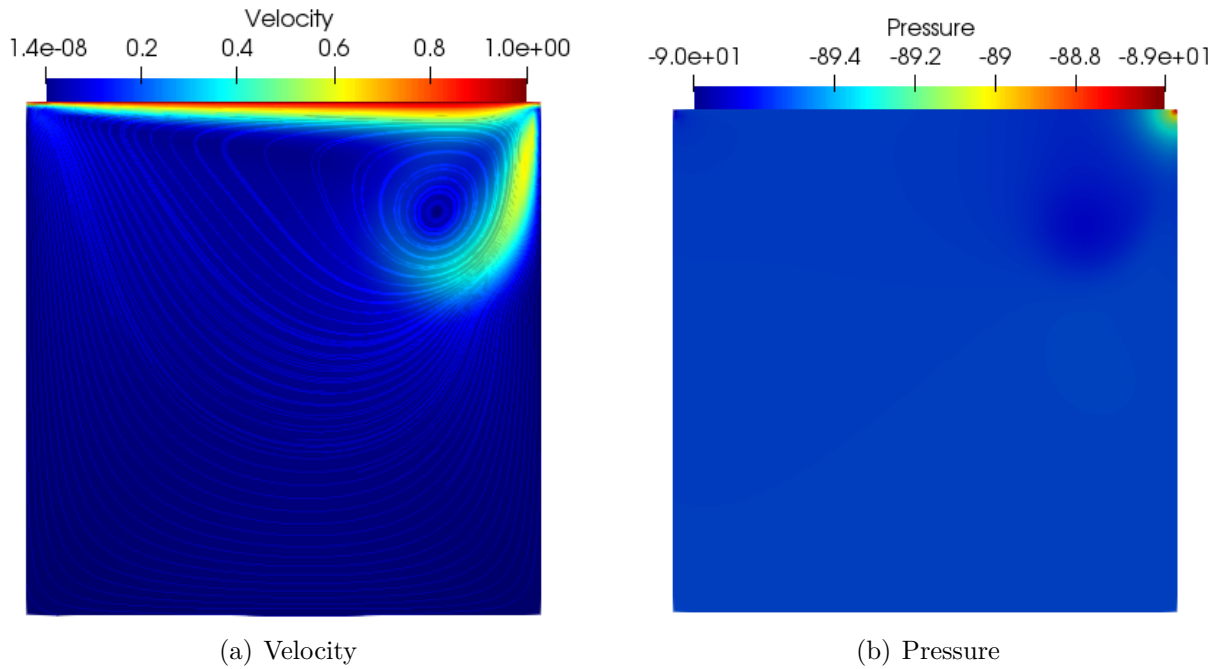


Figure 12 – Numerical simulation result of driven cavity problem at  $t = 2.5$  with  $Re=1000$ .

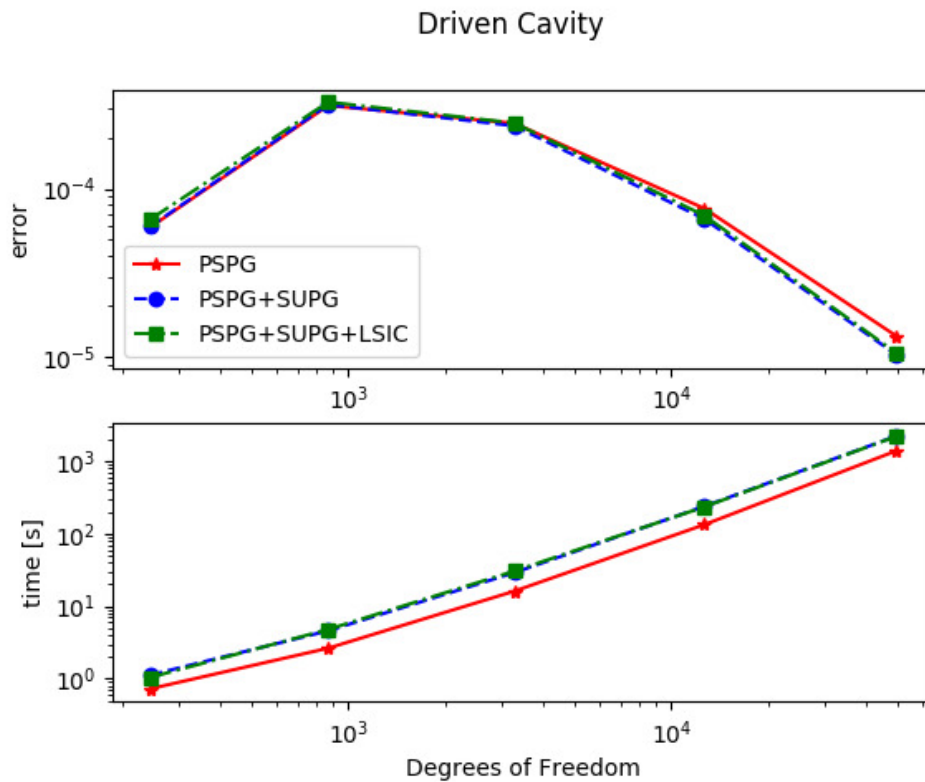


Figure 13 – Simulation analysis of driven cavity problem.

Based on Figure 13, adding more terms does not increase the CPU time significantly, and also, the errors are very similar. Since this problem has a  $Re = 1000$ , it is possible to see that the SUPG has increased the accuracy, as expected since this stabilization

was made for convective dominant problems. However, since the problem is still laminar, without sharp velocity gradients, the term LSIC did not influence the result significantly.

### 5.2.2 Pressure Driven

This second test problem is described in [8]. The pressure driven channel is chosen, as we seek the solution of the NSE in a benchmark where the flow occurs because of a difference pressure imposed as boundary conditions. The geometry of this problem is also a square cavity with sides of unit length and for this case, kinematic viscosity is set to  $\nu = 1/8$  [8]. In the upper and lower wall, a no-slip boundary condition is imposed and pressure Dirichlet BC is imposed as inflow and outflow conditions  $p(0, y) = 1$  and  $p(1, y) = 0$ . The initial velocity  $\mathbf{u}_0$  is set to zero. The functional of interest is  $u_i$  in the point  $(1.0, 0.5)$  at the final time. This problem is important because a reference value can be mathematically given by a Fourier series, which is rare in fluid dynamics [8].

$$u_i(1.0, 0.5, t) = 1 - \sum_{n=1,3,\dots}^{\infty} \frac{32}{\pi^3 n^3} e^{-\frac{\pi^2 n^2 t}{8}} (-1)^{(n-1)/2}, \quad (5.4)$$

for  $t = 0.5$ , the reference value is  $u_i \approx 0.443211$  [34].

Figure 14 shows the performed numerical results of velocity and pressure fields for time  $t = 0.5$ .

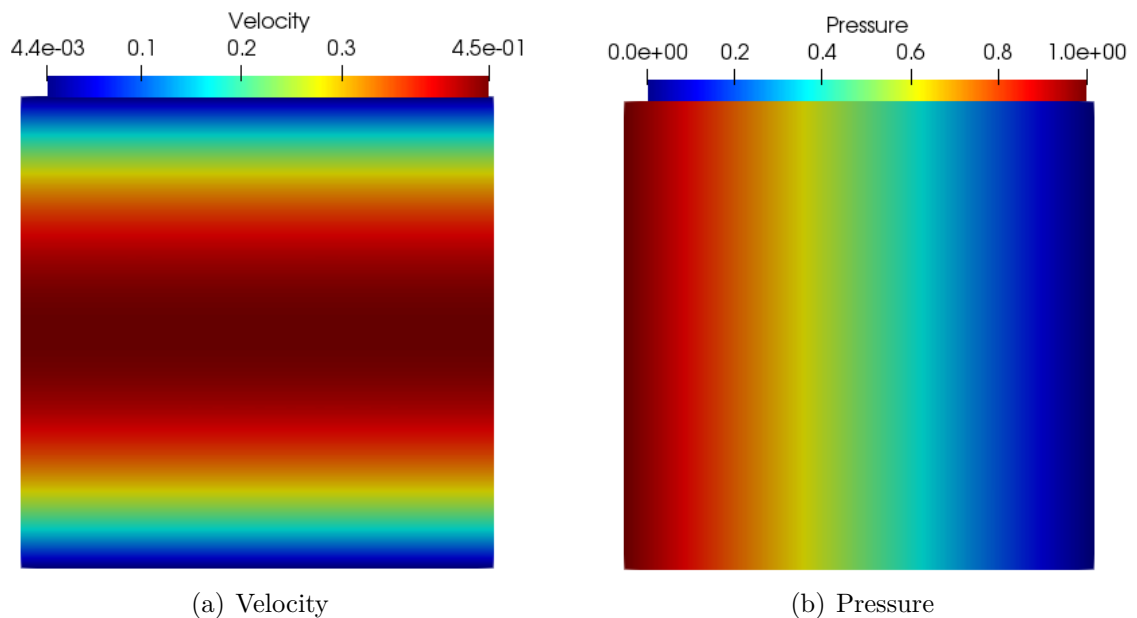


Figure 14 – Numerical results of the pressure driven problem at  $t = 0.5$ .

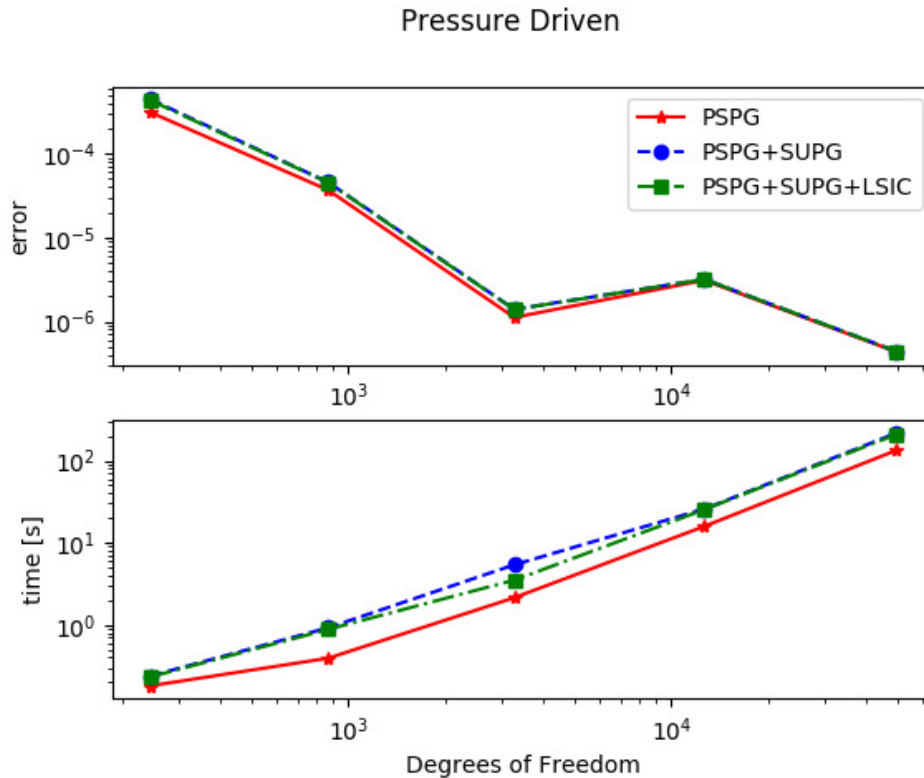


Figure 15 – Simulation analysis of the pressure driven problem.

Figure 15 shows the error and CPU time of the pressure driven problem. For this specific problem, since the Reynolds number is so small that is no need for using SUPG or LSIC stabilizations since it is not a convective neither turbulent problem. So it is possible to see that the error is almost the same since the other terms did not change the result significantly. However, they have increased the complexity, impacting in the CPU time.

### 5.2.3 Taylor-Green vortex

In this next test problem, a periodic flow with exact solution is chosen. This problem is described in [8] and [69]. The problem domain is  $[-1, 1] \times [-1, 1]$ , kinematic viscosity is set to  $\nu = 1/100$  and periodic boundary conditions are imposed in both the  $x$  and  $y$  directions. The functional of interest is the kinetic energy  $K = \frac{1}{2} \|u\|_{L^2}^2$  at final time  $T = 0.5$ . The exact solutions of this problem is given by [8]:

$$\mathbf{u}(x, y, t) = (\cos(\pi x) \sin(\pi y) e^{-2t\nu\pi^2}, \cos(\pi y) \sin(\pi x) e^{-2t\nu\pi^2}),$$

$$p(x, y, t) = -0.25(\cos(2\pi x) + \cos(2\pi y)) e^{-4t\nu\pi^2}.$$

Figure 16 shows the initial values of pressure and velocity fields and in Figure 17, the numerical result for both fields at  $t = 0.5$  is presented.

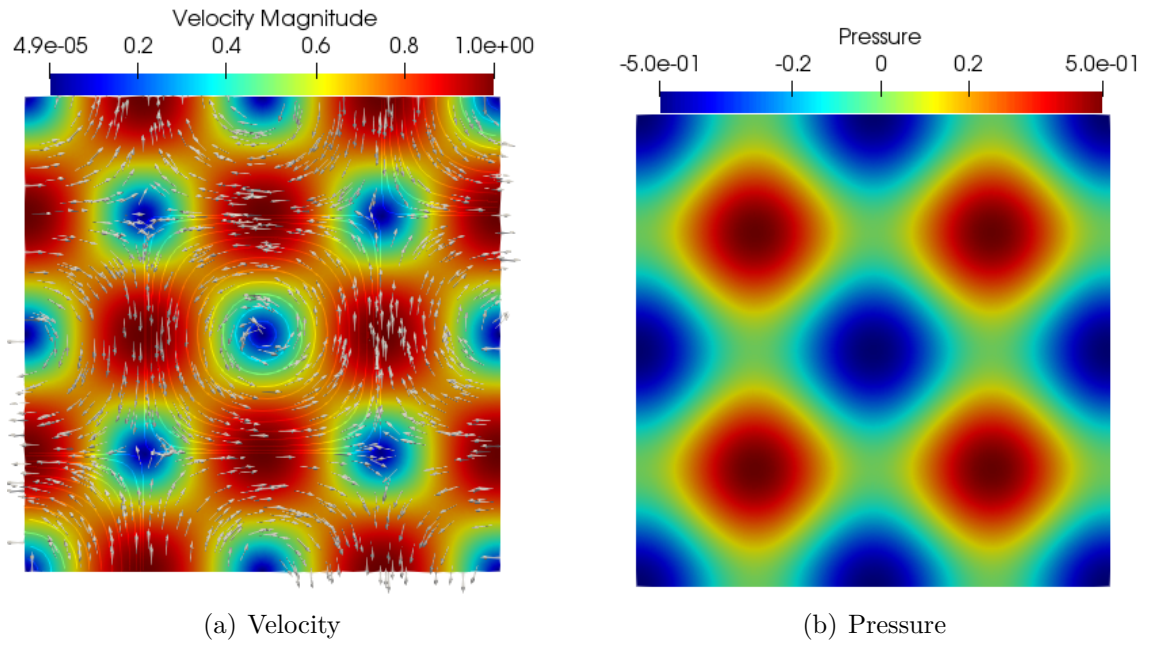


Figure 16 – Initial conditions of the Taylor-Green vortex problem [8].

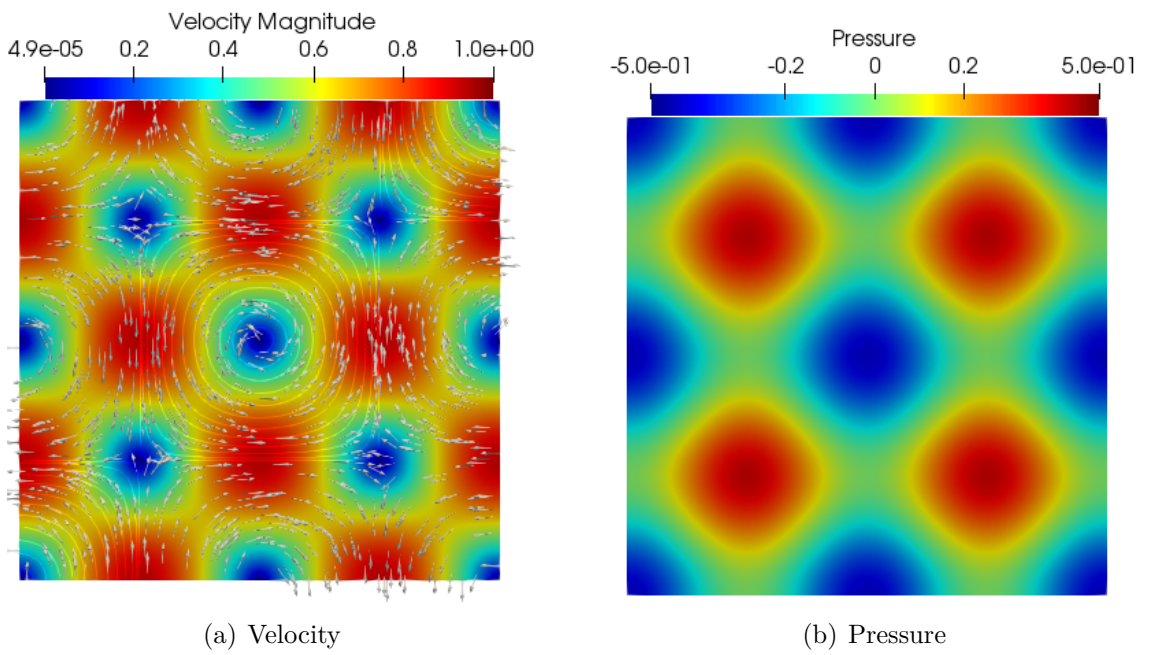


Figure 17 – Numerical simulations of Taylor-Green vortex problem at  $t = 0.5$ .

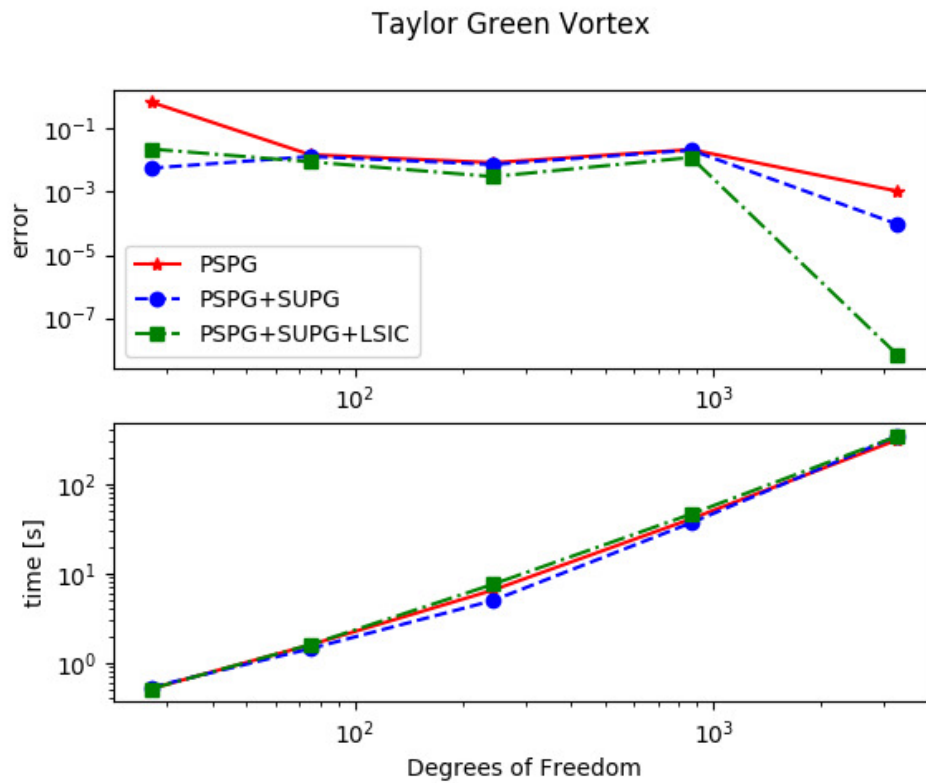


Figure 18 – Simulation analysis of Taylor-Green Vortex problem.

For the Taylor-Green vortex problem, Figure 18 shows the error and CPU time. For this problem, the most accurate method is the stabilization PSPG+SUPG+LSIC, due to the complex flow with several vortices. Further, the CPU time is almost the same for all cases.

#### 5.2.4 Flow past a cylinder

For this last problem, it is considered the flow past a cylinder. This is well discussed in [70] and it is a very usual test problem to simulate flows with moderate to high Reynolds number due to the unstable flow generated with the presence of high velocity and an obstacle. The problem geometry can be visualized on Figure 19.

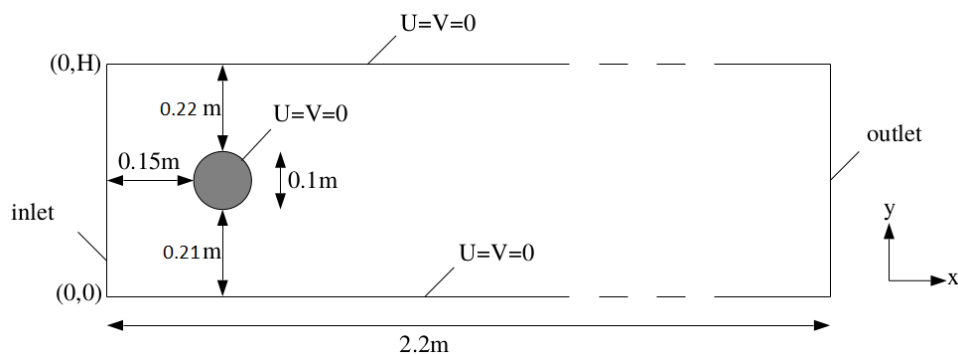


Figure 19 – Flow past a cylinder geometry.

The cylinder is slightly displaced from the center of the channel and the resulting flow is a vortex street forming behind the cylinder. No-slip boundary conditions are applied to the cylinder as well as the upper and lower walls of the channel. A zero Dirichlet boundary condition is imposed on the pressure at the outlet. The inflow velocity is a time-varying parabolic profile given by [8]:

$$\mathbf{u}(0, y, t) = (4U_m y(H - y) \sin(\pi t/8)/H^4, 0), \quad (5.5)$$

where  $U_m = 1.5$  and  $H = 0.41$ . The kinematic viscosity is  $\nu = 1/1000$ . As a functional of interest, it is considered the pressure difference between the front and back of the cylinder at the final time  $T = 8$ :

$$\Delta p = p(0.45, 0.2, 8) - p(0.55, 0.2, 8).$$

In according with [8], this pressure difference is  $\Delta p = -0.11144$ . Figures 20 and 21 show the velocity and pressure fields obtained on the simulations.

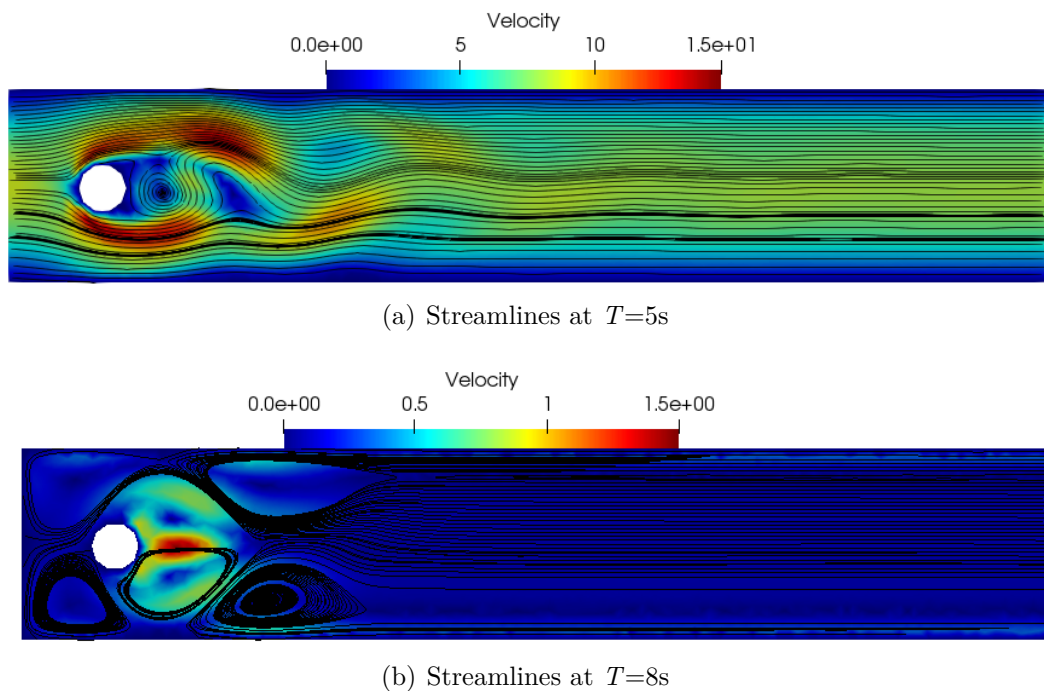


Figure 20 – Stream line simulation result of flow around a cylinder problem.

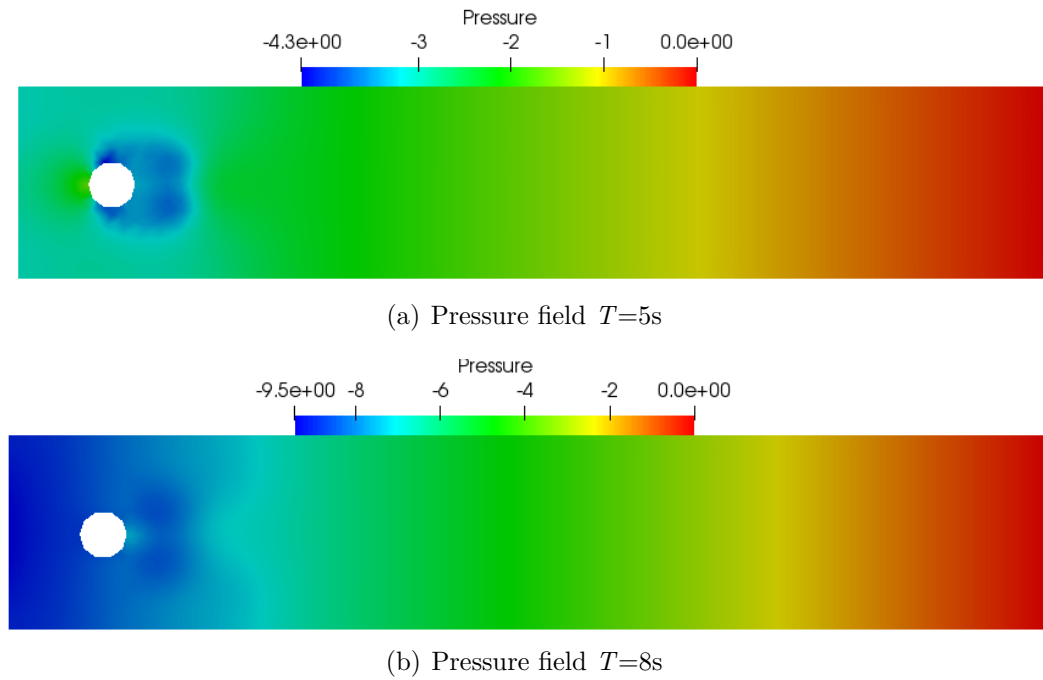


Figure 21 – Pressure simulation result of flow around a cylinder problem.

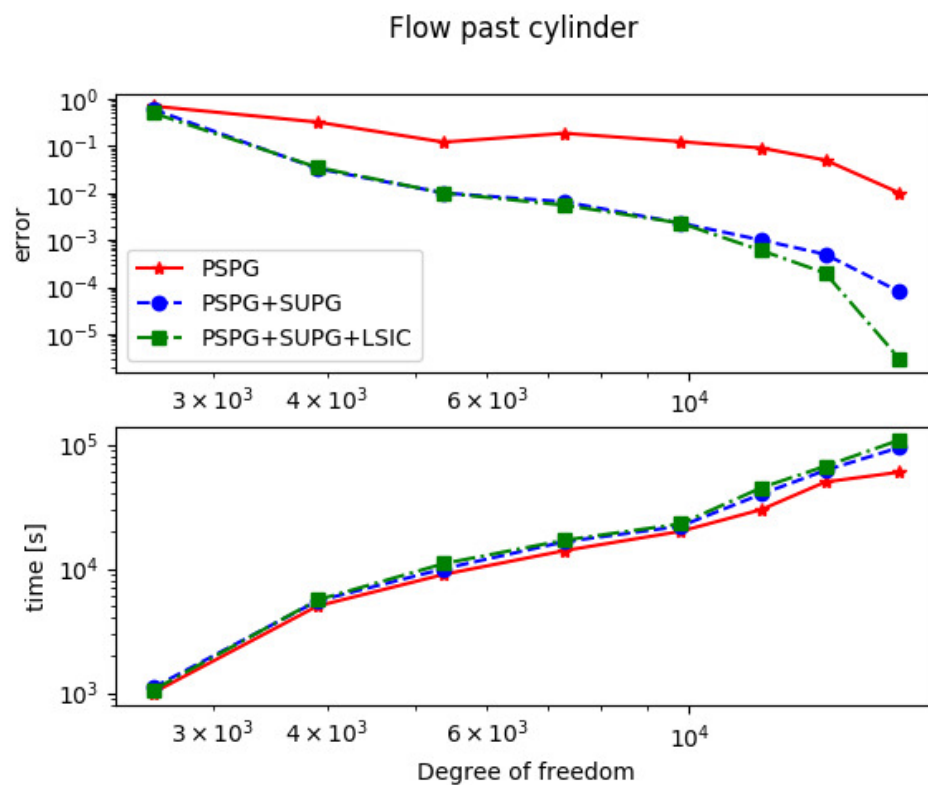


Figure 22 – Simulation analysis of flow around a cylinder problem.

For the flow around a cylinder problem, Figure 22 shows that the stabilized method SUPG increases remarkably well the problem accuracy, and since the problem has a higher

$Re$ , the LSIC have also demonstrated to increase accuracy for refined meshes. For this problem, stabilization pure PSPG is not recommended.

#### 5.2.5 Conclusions on FEniCS for fluid problems

Evaluating the graphics plots for error and CPU time of each problem discussed in Section 5.2 it is possible to define FEniCS as a useful library to solve fluid problems using FEM, discussed in Section 4.1.

Concerning method selection, if the problem has a restriction about the polynomial order, as is the case of the CMM-FSI, the use of the stabilization PSPG is mandatory. The SUPG stabilization must be used for convective dominant problems, as it is the most of the cases of fluid dynamics problems in this work. The LSIC is used for turbulent flows, which is not the focuses here.

## 6 ARTERIAL BLOOD FLOW

Finally, this chapter is dedicated to the hemodynamic study. Therefore, this study will be performed in idealized large arteries geometries, constructed upon real physiological data. At first, a validation of the implemented fluid-structure model is performed. After, an idealized model of the carotid artery, described in [7], is used to study the blood pressure and flow wave and perform a comparison between rigid and deformable models. The CMM-FSI then is used to perform a study into an idealized model of the common carotid artery, with stenosis. The constitutive parameters for fluid (blood) and solid (blood vessel) for all studies are presented in Table 3.

$\rho$	$\mu$	$E$	$\rho^s$	$\nu^s$	$k$	$\zeta$
$g/cm^3$	$dyn.s/cm^2$	$dyn/cm^2$	$g/cm^3$	-	-	$cm$
1.06	0.04	$4.07 \times 10^6$	1.09	0.5	5/6	0.03

Table 3 – Blood and artery wall parameters. Taken from [7].

### 6.1 FLUID-STRUCTURE MODEL VALIDATION

A simple cylindrical model with a nominal radius and vessel length of 0.3 cm and 4.2 cm, respectively, is used. The mesh was generated in the FEniCS with the *mshr* library and it has 24067 elements and 4782 nodes (see Figure 23).

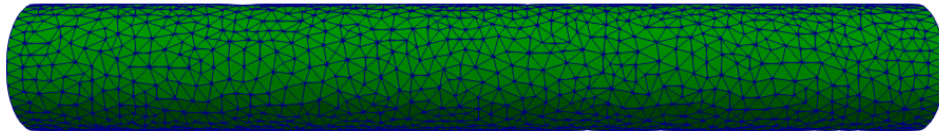


Figure 23 – Mesh visualization of an idealized vessel.

A steady-state parabolic velocity profile is assigned to the inlet boundary. For the outlet boundary, it is prescribed a constant pressure of  $1330 \text{ dyn/cm}^2$ . The behavior of the fluid-structure model is validated in comparison with the blood flow theory by Poiseuille, given by [34]:

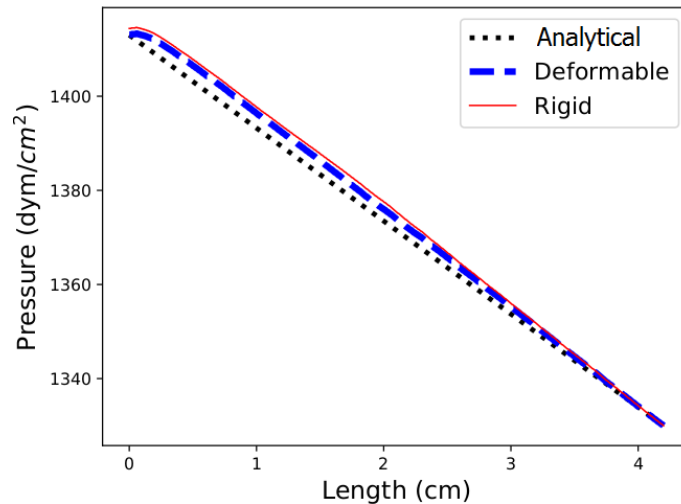
$$p(x) = p_0 + cx, \quad (6.1)$$

$$v(r) = V_{max} \left( 1 - (r/R)^2 \right). \quad (6.2)$$

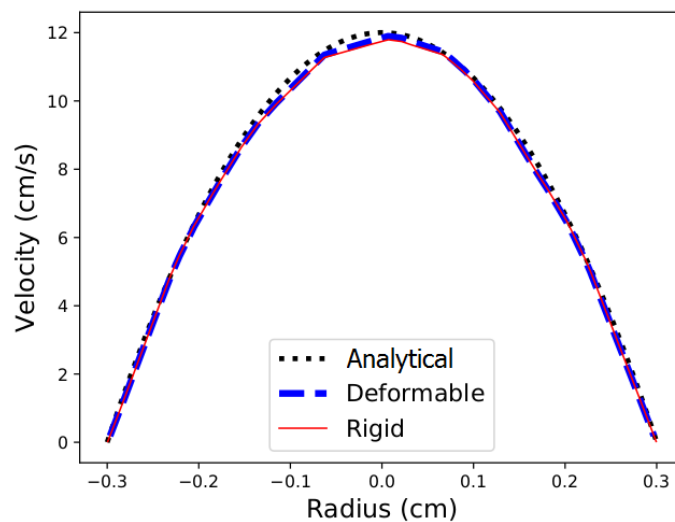
These equations relate the pressure and the flow rate in a pipe for a steady-state flow with low dynamic viscosity, where  $p_0 = 1413 \text{ dyn/cm}^2$ ,  $c = -19.76 \text{ dyn/cm}^3$  is the axial pressure gradient,  $R$  is the artery radius,  $r$  is the radial distance and  $V_{max} = 12.5 \text{ cm/s}$  is

the maximum velocity, found at the inlet centerline. With those parameters, using the equation (3.1), we found  $Re = 99.38$ .

The numerical simulation started from initial conditions of velocity and pressure equal to zero for the rigid problem. The velocity  $\mathbf{u}^0$  and pressure  $p^0$  fields obtained in the rigid case are then used as initial conditions for the deformable wall problem. The simulation was performed until the steady-state condition, which happens after the relative velocity norm reaches a pre-set tolerance of  $10^{-5}$  in order to compare with Poiseuille equation [6]. Once reached, the wall must have a small relative displacement of order  $10^{-3}$  that does not change the flow profile and pressure decay. Figure 24 compares the rigid and deformable case of a fully converged steady flow solution with the theoretical Poiseuille equation. The parabolic profile with near-zero value in the walls (-0.3 and 0.3) for the velocity and linear decay through the length for the pressure results demonstrate the correct behavior for both models.



(a) Pressure over length



(b) Velocity versus radius at the center ( $x = 2.1$  cm)

Figure 24 – Comparisons between rigid and deformable models against theoretical function.

Figure 25 represents the wall displacement and the blood flow streamlines for the initial and final phases of the simulation. The initial displacement is found by loading the vessel wall with a body force  $\mathbf{b}^s$  estimated to be the average value of the pressure in the interface  $\mathcal{P}$ , obtained by using the pressure field  $p^0$  from the rigid case. The radial displacement for the next time steps is then calculated using the Newmark's formula presented in Section 4.1.1 and after reaching the steady-state condition, the displacement field  $\mathbf{v}$  must be next to zero with a tolerance of  $10^{-3}$ . A radial displacement of  $0.0005 \text{ cm}$  was found in this study, as shown in Figure 25b. Moreover, a maximum radial displacement of  $0.0017 \text{ cm}$  is found, equivalent to a 1.13% deformation. These results are in agreement with such that a maximum deformation of 5% is obtained with a physiologic range of pressures, discussed in Section 2.1 and in agreement with [37].

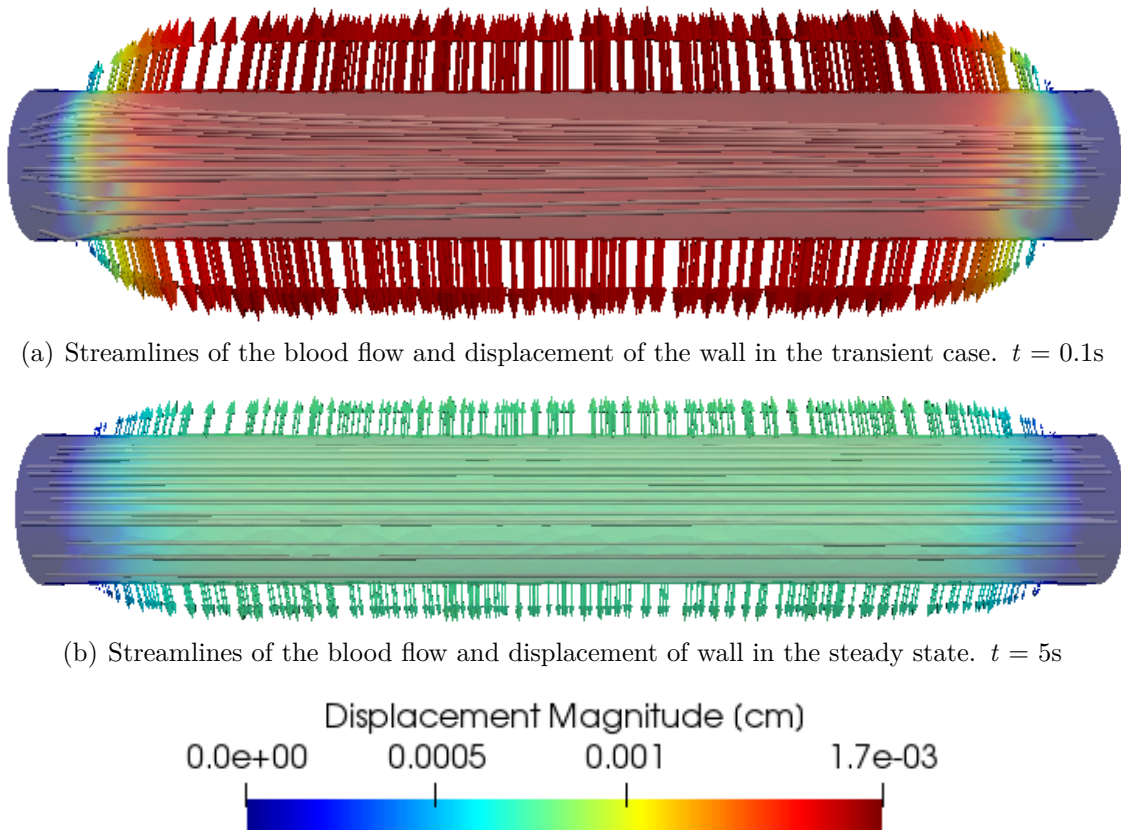


Figure 25 – Wall displacement.

## 6.2 BLOOD FLOW AND PRESSURE WAVES

In this section, we perform a study in the blood flow and pressure waves. Pulsatile inflow condition is used in reason to observe the wave propagation and difference between pressure spikes phenomena in both models. For this purpose, a manufactured common carotid artery, discussed in Section 2.1.4, which is a simple cylindrical model with nominal radius and vessel length of  $0.3 \text{ cm}$  and  $12.6 \text{ cm}$  respectively, is used [7]. A mesh with 38897

elements and 8178 nodes was made with FEniCS and *mshr* to perform the simulations (see Figure 26).

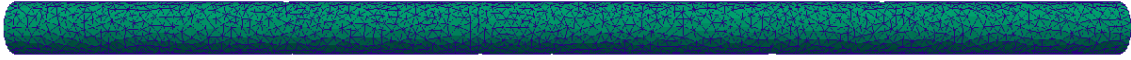


Figure 26 – Mesh visualization for idealized common carotid.

Initially, sinusoidal inflow is used to model a simplified pulsatile flow caused by the heart pulse. This pulse has a period of  $T = 0.6$  s and the parabolic profile is kept, with a mean velocity of  $V_m = 12.5$  cm/s. A fixed pressure  $P = 1330$  dyn/cm<sup>2</sup> is applied for outlet boundary. The maximum Reynolds number found if this problem is  $Re = 99.38$ . The expression for velocity is given by [34]:

$$v(r, t) = \frac{V_m(r^2 - y^2 - z^2)}{r^2}(1 + \sin(2\pi t/T)). \quad (6.3)$$

Figure 27 shows how both models have similar behavior. However, the differences in both the pressure and flow waves between the rigid and deformable wall solutions are discernible. The pressure difference, in the sinusoidal case,  $\Delta p = 2387.29 - 2250.26 = 137.03$  dyn/cm<sup>2</sup>, showing higher values in systoles (peaks) and lower in diastole (valley). For the velocity field or flow wave, the phase lag, i.e. the time difference between the peaks or valleys, is  $0.67922 - 0.666507 = 0.0127$  s. On another hand, the effects of the phase lag are hard to determine within this computation.

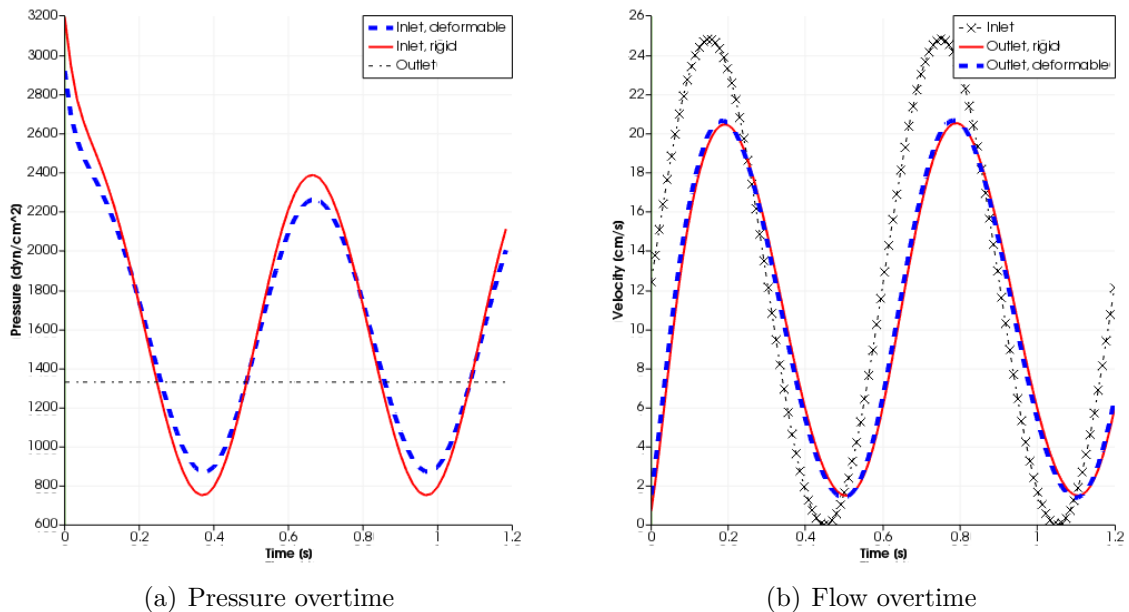


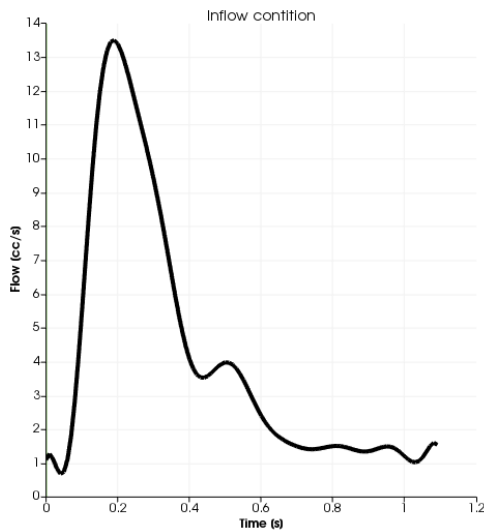
Figure 27 – Sinusoidal model: Pressure and velocity for 2 cycles.

### 6.2.1 Rigid versus deformable model: a comparative study

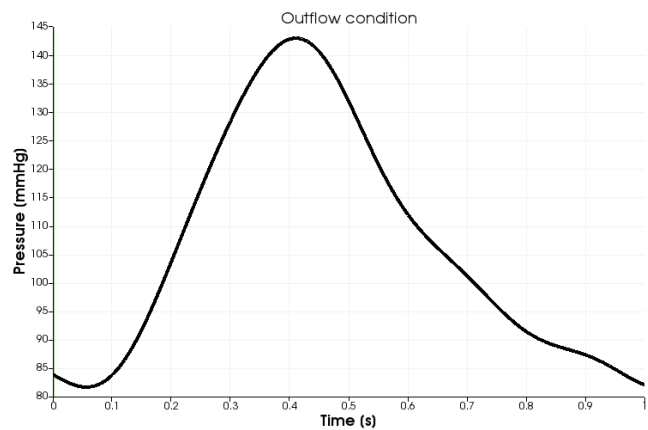
Since some effects of the FSI model was hard to determine within the sinusoidal study, for a more in-depth comparison between rigid and deformable wall models, this section presents a combination between the parabolic periodic flow wave (Figure 29a) [71] with two different outlet conditions: a pressure of  $100 \text{ mmHg}$  (constant) and blood pressure wave for a  $145 - 80 \text{ mmHg}$  pressure with  $60 \text{ bpm}$  heart frequency (Figure 29b) [72]. Figure 28 shows the sections (S1 and S2), which were used to evaluate the comparison. Those planes are located  $0.6 \text{ cm}$  distant from the inlet and outlet faces. These locations were chosen since they are far enough from the inlet and outlet (where the nodes on the wall are kept fixed) so the radial deformation is not affected by the presence of the boundary.



Figure 28 – Planes S1 and S2 of evaluation. Adapted from [7].



(a) Blood flow wave



(b) Blood pressure wave

Figure 29 – Pressure and blood flow waves at the outlet and inlet faces, respectively.  $1 \text{ cc} = 10^{-6} \text{ m}^3$ .

Figure 30 shows that the pressure field and flow waves have a discernible solution for each case. For the pressure field, Figure 30d, display that pressures obtained with rigid wall models present a higher pressure pulse value. As described in [26], this pressure difference of  $\Delta p = 145.18 - 134.53 = 10.65 \text{ mmHg}$  is a well-known phenomenon in the cardiovascular system, where stiffer vessels tend to experience higher pressure pulses, showing higher values in systoles (peaks) and lower in diastole (valley). On the other hand,

Figure 30c does not present this expected result. Figueroa *et al.* [7] explain that some outflow boundary conditions, as probably this case, generate unrealistic high-pressure pulses in deformable models.

The velocity field also presents noticeable differences. First of all, it is possible to notice a phase lag of  $0.015s$  between the rigid and deformable waves in Figure 30a, provided by the wave propagation phenomena. This phase lag provides a means to estimate the pulse velocity [73]. Considering that the vessel length is  $12.6\text{ cm}$ , this produces a pulse velocity of approximately  $840\text{ cm/s}$ , in agreement with the speed range discussed in Section 2.1, but relatively higher than the speed found by [7]. This is probably because of the different outflow conditions used in each study. The maximum Reynolds number found in this problem is  $Re = 108$ .

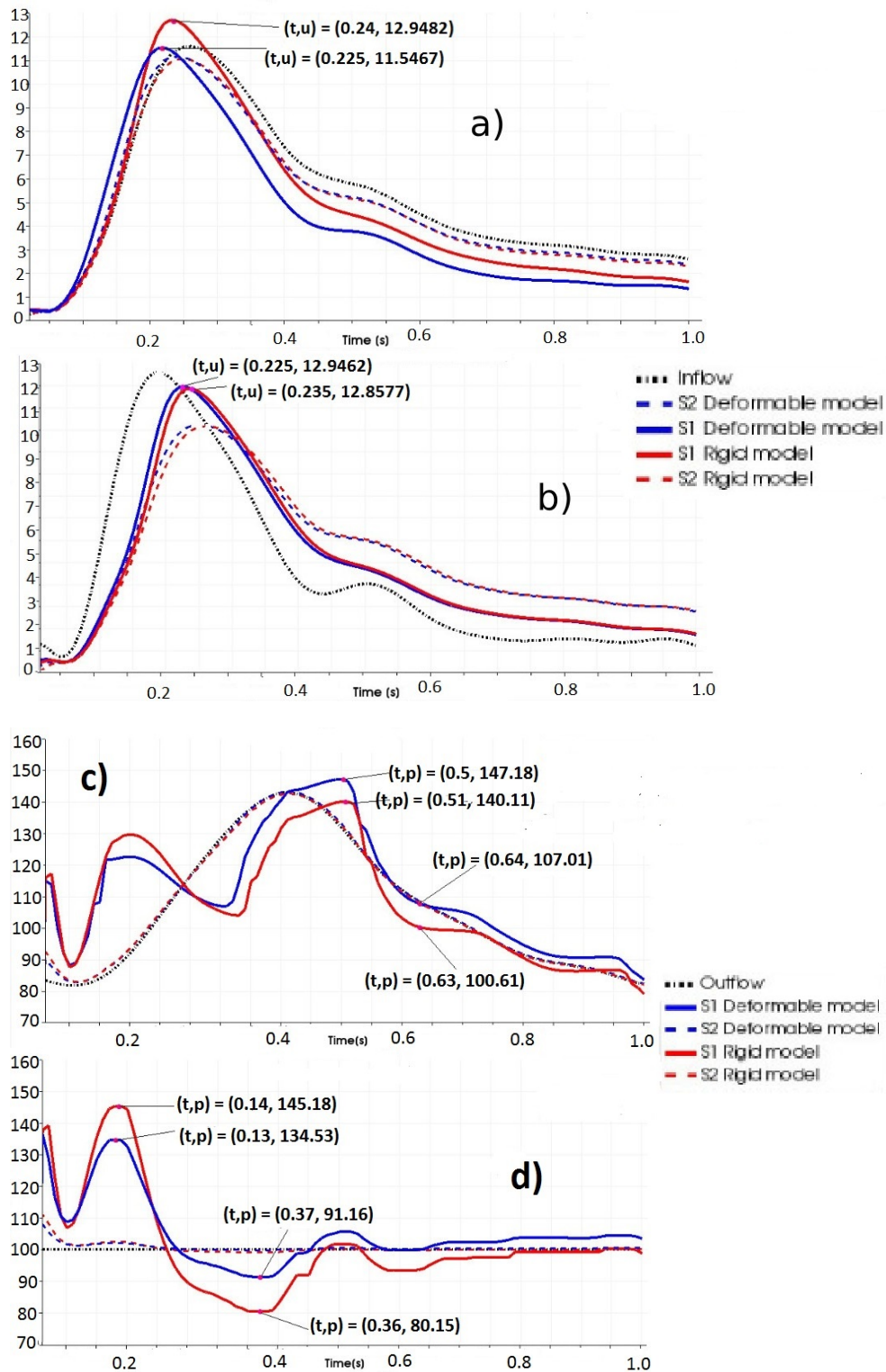


Figure 30 – Comparison between rigid and deformable models. Plots (a) and (b) are the flow overtime for a pressure wave and fixed pressure respectively. Plots (c) and (d) are the pressure overtime for pressure wave BC and fixed pressure respectively.

Finally, Figure 31 shows that the displacement has different behavior for each model, for both its dynamics and magnitude. Positive and negative values mean outside

and inside radial directions, respectively. Moreover, the maximum radial displacement is  $0.007\text{ cm}$  and it is equivalent to 2.33% deformation.

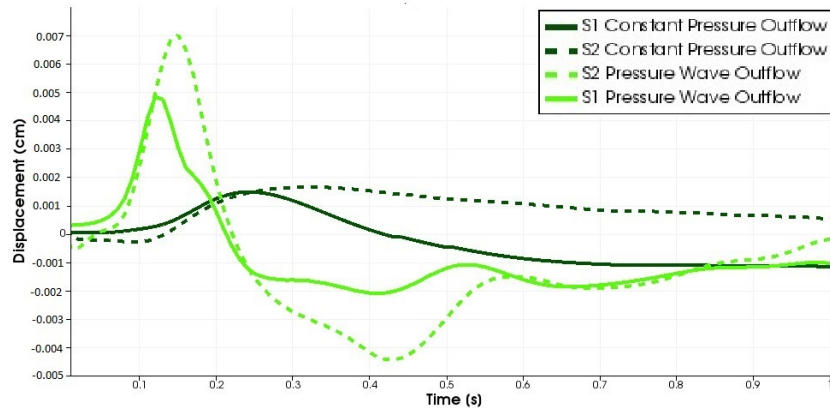


Figure 31 – Radial displacement in S1 and S2 for the carotid artery model using constant pressure BC and pressure wave BC.

### 6.3 FLOW IN A STENOSED COMMON CAROTID ARTERY

Here we are interested in simulating the blood flow in a stenosed common carotid artery. Figure 32 presents the model geometry, taken from [7]. Here we are considering a  $126\text{ mm}$  long and  $6\text{ mm}$  diameter artery. The stenosis area is located  $25\text{ mm}$  from the inlet boundary and reduces in 75% the area.

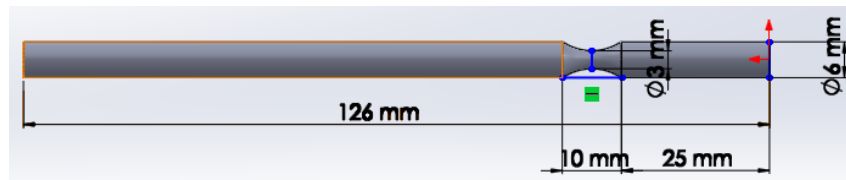


Figure 32 – Stenosis geometry of the carotid artery.

This problem demands a finer mesh due to the higher velocity created in the divergent-convergent channel of the stenosis, which decreases the flow pressure and increases flow velocity. The geometry was generated using a CAD software *Solidworks*, and the mesh was made with *GMSH*. The mesh is constituted by 91530 elements and 21073 nodes as illustrated by Figure 33.

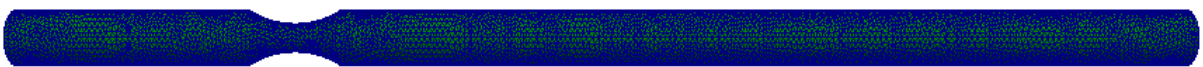


Figure 33 – Stenosis mesh for the carotid artery model.

This simulation was performed for 2 cardiac cycles, which means that the simulation occurred by repeating the boundary conditions of Figure 29 twice. This was done because

in some simulations results, the first cycle exhibit some numerical instabilities. Figure 34 shows the simulation results of the last cycle for the pressure, blood velocity and wall velocity for two cases: a peak of systole (0.2 s) and the mid diastole (0.9 s). The pressure drop along the vessel is approximated 5 *mmHg* during most of the diastole, reaching approximating 20 *mmHg* during the systole peak. Those results are in agreement with the physiological range of pressure of 80-130 *mmHg*.

As expected, the velocity is increased after the stenosed area in about 50 *cm/s* during the peak of systole. The wall velocity is much higher at the systole, experiencing about 0.7 *cm/s* at the center of the stenosed area, but really low values at the mid diastole. This study was based on [7] and the results here obtained are in agreement with those. However, it is important to inform that Figueroa *et al.* [7] has considered an impedance outflow condition, that was not explicitly specified. The maximum Reynolds number found in this study, using the equation (3.1), was  $Re = 1590$ .

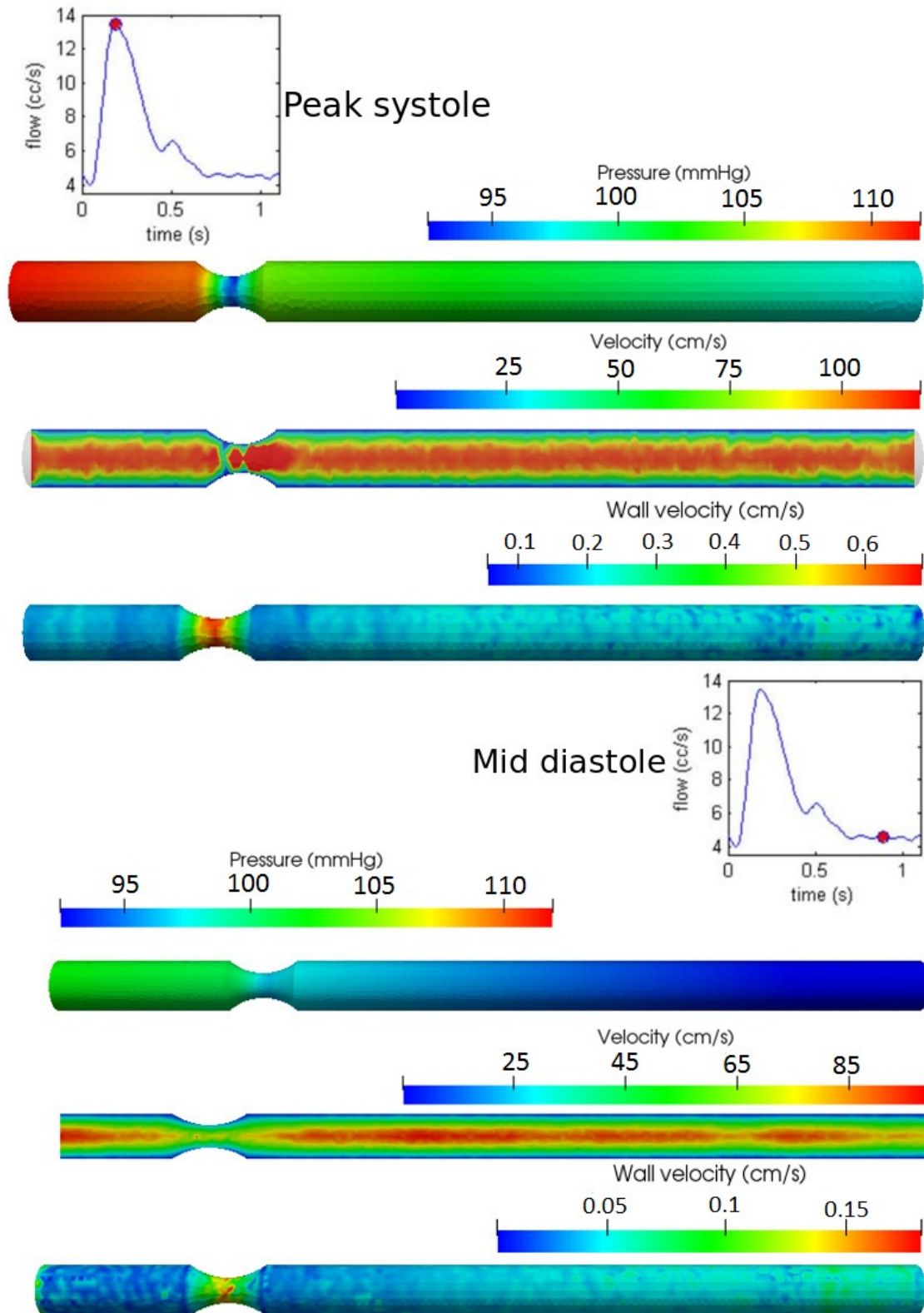


Figure 34 – Simulation result of the common carotid artery with stenosis. The results are pressure, blood velocity and wall velocity from top to bottom.

## 7 CONCLUSION

This work has successfully implemented and solved fluid dynamics problems using three different numerical methods and it also investigated 3D blood flow problems using a fluid-structure approach with the CMM-FSI. All problems were solved using the FEniCS library and the Python programming language. For the fluid dynamics problems, explored in Chapter 5, the goal was to understand fluid dynamics properties as the Reynolds number and how to implement and solve problems using FEniCS. Thus, four distinct problems were solved using different flow conditions, i.e., diverse boundary conditions, Reynolds numbers and domain geometries. Each problem was solved using the Galerkin method with PSPG, SUPG and LSIC stabilizations. As a method for evaluation, a comparison using CPU time and error for different mesh sizes was made. The PSPG is a stabilization necessary for the LBB condition, the SUPG has increased the numerical accuracy and the LSIC did not change the results significantly because none of the problems had a complete turbulent flow. Also, FEniCS has demonstrated to be a good and reliable library to solve fluid dynamics problems.

To investigate the blood flow in 3D deformable arteries, first Chapter 2 gave a brief introduction to the arterial system, circulation and blood rheology. The CMM-FSI was firstly tested against the Poiseuille's blood flow theory and also with a rigid wall assumption. The simulation of blood flow using an idealized artery, i.e., a simple pipe channel was performed until the steady-state, and the results were very similar to both rigid case and theoretical values. Thus, an idealized model of the common carotid artery was used to conduct a comparative study between rigid and deformable wall assumptions. For this study, real and physiological blood flow and pressure waves were used to represent a more realistic simulation. The results have demonstrated that for 3D geometric models, each model choice brings a different result, which should be analyzed. Therefore, since the pressure differences of both models are quite large, it is important to notice that even using a model that represents more realistic phenomena, the selection of physiological boundary conditions is mandatory.

The common carotid artery model was modified to a model with 75% reduced area stenosis. For this problem, it was expected to get a flow with high velocities after the reduced area, so a finer mesh was used. The results about blood pressure, blood velocity, and wall velocity are demonstrated for two different times of a cardiac circle: the peak of systole and the mid diastole. Even with this pathology, the range of pressures was similar to the previous health carotid artery model and the results were satisfactory when compared to the same study performed in the literature, even using a different outflow condition.

During the development of this work, the author had the opportunity to visit the

Simula Research Laboratory, Norway, in the Summer School of Computational Physiology. This amazing opportunity was essential for a greater understanding of physiology, numerical methods and especially a larger experience using FEniCS, which they have developed. The preliminary results were accepted in two conferences:

- Gaio, E.D., Queiroz, R.A.B. and Camata, J.J., "A Comparative Study of Numerical Schemes for Solving Navier Stokes Equations Using Flow Problems Benchmarks", *Workshop on Computational Modeling and Numerical Analysis*, Petrópolis - RJ, 2019.
- Gaio, E.D. *et al.* "Investigation on the blood flow in deformation vessels using stabilized finite element method", *XXII Encontro Nacional De Modelagem Computacional & X Encontro De Ciência E Tecnologia De Materiais*, Juiz de Fora - MG, 2019.

For future works, there is a great number of possibilities. First of all, the use of the impedance boundary conditions for outflow is an idea, due to the wave propagation phenomena be directly linked to this condition. For the study of pathologies as the stenosis and aneurysm, the use of Non-Newtonian rheology models is also an option because they may represent phenomena closer to physiology. Finally, more realistic boundary conditions and rheology models can be used together with the CMM-FSI to perform a patient-specific study, using a 3D model of some artery reconstructed from clinical images.

## REFERENCES

- [1] A. Quarteroni, A. Manzoni, and C. Vergara, “The cardiovascular system: mathematical modelling, numerical algorithms and clinical applications,” *Acta Numerica*, vol. 26, pp. 365–590, 2017.
- [2] M. F. O’Rourke, C. O’Brien, and T. Weber, “Arterial stiffness, wave reflection, wave amplification: basic concepts, principles of measurement and analysis in humans,” in *Blood Pressure and Arterial Wall Mechanics in Cardiovascular Diseases*, pp. 3–13, Springer, 2014.
- [3] M. A. Z. Valencia, *Methods for automation of vascular lesions detection in computed tomography images*. PhD thesis, 2011.
- [4] N. Hayashi, E. Hori, Y. Ohtani, O. Ohtani, N. Kuwayama, and S. Endo, “Surgical anatomy of the cervical carotid artery for carotid endarterectomy,” *Neurologia medico-chirurgica*, vol. 45, no. 1, pp. 25–30, 2005.
- [5] T. Sochi, “Non-newtonian rheology in blood circulation,” *arXiv preprint arXiv:1306.2067*, 2013.
- [6] R. W. Fox, A. T. McDonald, and P. J. Pritchard, “Introduction to fluid dynamics,” *John Wiley & Sons*, 2004.
- [7] C. A. Figueroa, I. E. Vignon-Clementel, K. E. Jansen, T. J. Hughes, and C. A. Taylor, “A coupled momentum method for modeling blood flow in three-dimensional deformable arteries,” *Computer methods in applied mechanics and engineering*, vol. 195, no. 41-43, pp. 5685–5706, 2006.
- [8] A. Logg, K.-A. Mardal, and G. Wells, *Automated solution of differential equations by the finite element method: The FEniCS book*, vol. 84. Springer Science & Business Media, 2012.
- [9] P. D. Morris, A. Narracott, H. von Tengg-Kobligk, D. A. S. Soto, S. Hsiao, A. Lungu, P. Evans, N. W. Bressloff, P. V. Lawford, D. R. Hose, *et al.*, “Computational fluid dynamics modelling in cardiovascular medicine,” *Heart*, vol. 102, no. 1, pp. 18–28, 2016.
- [10] R. N. Elias, *Estruturas De Dados Por Arestas Para A Simulação Paralela De Escoamentos Incompressíveis Pelo Método Estabilizado De Elementos Finitos*. PhD thesis, Tese de Doutorado, COPPE/UFRJ, Rio de Janeiro, RJ, Brasil, 2007.
- [11] Y. Bazilevs, K. Takizawa, and T. E. Tezduyar, *Computational fluid-structure interaction: methods and applications*. John Wiley & Sons, 2013.
- [12] K. Stein, R. Benney, V. Kalro, T. E. Tezduyar, J. Leonard, and M. Accorsi, “Parachute fluid–structure interactions: 3-d computation,” *Computer Methods in Applied Mechanics and Engineering*, vol. 190, no. 3-4, pp. 373–386, 2000.
- [13] H. C. Gomes, *Método dos elementos finitos com fronteiras imersas aplicado a problemas de dinâmica dos fluidos e interação fluido-estrutura*. PhD thesis, Universidade de São Paulo, 2013.

- [14] C. A. Taylor and C. Figueroa, “Patient-specific modeling of cardiovascular mechanics,” *Annual review of biomedical engineering*, vol. 11, pp. 109–134, 2009.
- [15] F. Van de Vosse and M. Van Dongen, “Cardiovascular fluid mechanics—lecture notes,” *Faculty of Applied Physics, Faculty of Mechanical Engineering, Eindhoven University of Technology, Eindhoven, Netherlands*, 1998.
- [16] B. Thomas and K. Sumam, “Blood flow in human arterial system—a review,” *Procedia Technology*, vol. 24, pp. 339–346, 2016.
- [17] M. W. Arnaudin and J. J. Mintzes, “Students’ alternative conceptions of the human circulatory system: A cross-age study,” *Science Education*, vol. 69, no. 5, pp. 721–733, 1985.
- [18] S. Mittal and T. E. Tezduyar, “Parallel finite element simulation of 3d incompressible flows: Fluid-structure interactions,” *International Journal for Numerical Methods in Fluids*, vol. 21, no. 10, pp. 933–953, 1995.
- [19] E. Kuhl, S. Hulshoff, and R. De Borst, “An arbitrary lagrangian eulerian finite-element approach for fluid–structure interaction phenomena,” *International journal for numerical methods in engineering*, vol. 57, no. 1, pp. 117–142, 2003.
- [20] S. Court and M. Fournié, “A fictitious domain finite element method for simulations of fluid–structure interactions: The navier–stokes equations coupled with a moving solid,” *Journal of Fluids and Structures*, vol. 55, pp. 398–408, 2015.
- [21] M. Bukač, S. Čanić, J. Tambača, and Y. Wang, “Fluid–structure interaction between pulsatile blood flow and a curved stented coronary artery on a beating heart: A four stent computational study,” *Computer Methods in Applied Mechanics and Engineering*, 2019.
- [22] T. Z. T.J.R. Hughes, W.K. Liu, “Lagrangian–eulerian finite element formulation for incompressible viscous flows,” *Comput. Methods Appl. Mech*, 1981.
- [23] J. H. J. Donea, S. Giuliani, “An arbitrary lagrangian–eulerian finite element method for transient dynamic fluid–structure interactions,” *Comput. Methods Appl. Mech*, 1982.
- [24] A. Figueroa, K. E. Jansen, T. J. Hughes, and C. A. Taylor, “A coupled momentum method to model blood flow in deformable arteries,” *Tsinghua University and Springer-Verlag*, 2004.
- [25] T. J. Hughes, *The finite element method: linear static and dynamic finite element analysis*. Courier Corporation, 1987.
- [26] C. Vlachopoulos, M. O’Rourke, and W. W. Nichols, *McDonald’s blood flow in arteries: theoretical, experimental and clinical principles*. CRC press, 2011.
- [27] G. Strang and G. J. Fix, *An analysis of the finite element method*, vol. 212. Prentice-hall Englewood Cliffs, NJ, 1973.
- [28] O. C. Zienkiewicz, R. L. Taylor, P. Nithiarasu, and J. Zhu, *The finite element method*, vol. 3. McGraw-hill London, 1977.

- [29] V. Girault and P.-A. Raviart, “Finite element approximation of the navier-stokes equations,” *Lecture Notes in Mathematics, Berlin Springer Verlag*, vol. 749, 1979.
- [30] F. Brezzi and M. Fortin, “Mixed and hybrid finite element methods,” vol. 15, 2012.
- [31] A. N. Brooks and T. J. Hughes, “Streamline upwind/petrov-galerkin formulations for convection dominated flows with particular emphasis on the incompressible navier-stokes equations,” *Computer methods in applied mechanics and engineering*, vol. 32, no. 1-3, pp. 199–259, 1982.
- [32] T. E. Tezduyar, “Stabilized finite element formulations for incompressible flow computations,” in *Advances in applied mechanics*, vol. 28, pp. 1–44, Elsevier, 1991.
- [33] T. E. Tezduyar and Y. Osawa, “Finite element stabilization parameters computed from element matrices and vectors,” *Computer Methods in Applied Mechanics and Engineering*, vol. 190, no. 3-4, pp. 411–430, 2000.
- [34] F. M. ABREU, “Simulações numéricas de problemas descritos pelas equações de navier-stokes incompressíveis via biblioteca fenics,” Master’s thesis, Universidade Federal do Espírito Santo, 2017.
- [35] D. Mozaffarian, E. J. Benjamin, A. S. Go, D. K. Arnett, M. J. Blaha, M. Cushman, S. R. Das, S. De Ferranti, J. P. Després, H. J. Fullerton, *et al.*, “Heart disease and stroke statistics-2016 update a report from the american heart association,” *Circulation*, vol. 133, no. 4, pp. e38–e48, 2016.
- [36] A. H. Association *et al.*, “Heart disease and stroke statistics: 2017 at-a-glance,” 2017.
- [37] S. Glagov, C. Zarins, D. P. Giddens, and D. N. Ku, “Hemodynamics and atherosclerosis. insights and perspectives gained from studies of human arteries.,” *Archives of pathology & laboratory medicine*, vol. 112, no. 10, pp. 1018–1031, 1988.
- [38] W. S. Moore, *Vascular surgery: a comprehensive review*. WB Saunders Company, 2002.
- [39] M. Oshima, R. Torii, T. Kobayashi, N. Taniguchi, and K. Takagi, “Finite element simulation of blood flow in the cerebral artery,” *Computer methods in applied mechanics and engineering*, vol. 191, no. 6-7, pp. 661–671, 2001.
- [40] J. R. Cezbral, M. A. Castro, O. Soto, R. Löhner, and N. Alperin, “Blood-flow models of the circle of willis from magnetic resonance data,” *Journal of Engineering Mathematics*, vol. 47, no. 3-4, pp. 369–386, 2003.
- [41] M. Shojima, M. Oshima, K. Takagi, R. Torii, M. Hayakawa, K. Katada, A. Morita, and T. Kirino, “Magnitude and role of wall shear stress on cerebral aneurysm: computational fluid dynamic study of 20 middle cerebral artery aneurysms,” *Stroke*, vol. 35, no. 11, pp. 2500–2505, 2004.
- [42] L. B. Van, A. Hoeks, M. Kool, and H. A. Struijker-Boudier, “Introduction to large artery properties as a target for risk reduction by antihypertensive therapy.,” *Journal of hypertension. Supplement: official journal of the International Society of Hypertension*, vol. 10, no. 6, pp. S123–6, 1992.

- [43] P. Chaturani and R. Ponnalagar Samy, “A study of non-newtonian aspects of blood flow through stenosed arteries and its applications in arterial diseases,” *Biorheology*, vol. 22, no. 6, pp. 521–531, 1985.
- [44] A. Quarteroni, M. Tuveri, and A. Veneziani, “Computational vascular fluid dynamics: problems, models and methods,” *Computing and Visualization in Science*, vol. 2, no. 4, pp. 163–197, 2000.
- [45] L. Formaggia, A. Quarteroni, and A. Veneziani, *Cardiovascular Mathematics: Modeling and simulation of the circulatory system*, vol. 1. Springer Science & Business Media, 2010.
- [46] P. Pathmanathan, S. Chapman, D. Gavaghan, and J. Whiteley, “Cardiac electromechanics: the effect of contraction model on the mathematical problem and accuracy of the numerical scheme,” *The Quarterly Journal of Mechanics & Applied Mathematics*, vol. 63, no. 3, pp. 375–399, 2010.
- [47] C. Dewey, S. Bussolari, M. Gimbrone, and P. F. Davies, “The dynamic response of vascular endothelial cells to fluid shear stress,” *Journal of biomechanical engineering*, vol. 103, no. 3, pp. 177–185, 1981.
- [48] E. L. Yellin, “Laminar-turbulent transition process in pulsatile flow,” *Circulation research*, vol. 19, no. 4, pp. 791–804, 1966.
- [49] M. G. Larson and F. Bengzon, *The finite element method: theory, implementation, and applications*, vol. 10. Springer Science & Business Media, 2013.
- [50] S. Seshadhri, G. Janiga, O. Beuing, M. Skalej, and D. Thévenin, “Impact of stents and flow diverters on hemodynamics in idealized aneurysm models,” *Journal of biomechanical engineering*, vol. 133, no. 7, p. 071005, 2011.
- [51] A. I. Barakat and E. T. Cheng, “Numerical simulation of fluid mechanical disturbance induced by intravascular stents,” in *Proceedings of the 11th International Conference on Mechanics in Medicine and Biology*, pp. 2–5, 2000.
- [52] J. T. Ottesen, M. S. Olufsen, and J. K. Larsen, *Applied mathematical models in human physiology*. SIAM, 2004.
- [53] F. G. Basombrío, E. A. Dari, G. C. Buscaglia, and R. A. Feijóo, “Numerical experiments in complex haemodynamic flows. non-newtonian effects,” *International Journal of Computational Fluid Dynamics*, vol. 16, no. 4, pp. 231–246, 2002.
- [54] M. Toloui, B. Firoozabadi, and M. Saidi, “A numerical study of the effects of blood rheology and vessel deformability on the hemodynamics of carotid bifurcation,” *Scientia Iranica*, vol. 19, no. 1, pp. 119–126, 2012.
- [55] J. Janela, A. Moura, and A. Sequeira, “A 3d non-newtonian fluid–structure interaction model for blood flow in arteries,” *Journal of Computational and Applied Mathematics*, vol. 234, no. 9, pp. 2783–2791, 2010.
- [56] W. S. Slaughter, “Linearized elasticity problems,” in *The Linearized Theory of Elasticity*, pp. 221–254, Springer, 2002.

- [57] J. Zhou and Y. Fung, “The degree of nonlinearity and anisotropy of blood vessel elasticity,” *Proceedings of the National Academy of Sciences*, vol. 94, no. 26, pp. 14255–14260, 1997.
- [58] T. J. Hughes, *The finite element method: linear static and dynamic finite element analysis*. Courier Corporation, 2012.
- [59] R. D. Cook *et al.*, *Concepts and applications of finite element analysis*. John Wiley & Sons, 2007.
- [60] C. Felippa, “A historical outline of matrix structural analysis,” 2001.
- [61] S. Brenner and R. Scott, *The mathematical theory of finite element methods*, vol. 15. Springer Science & Business Media, 2007.
- [62] F. Brezzi, “On the existence, uniqueness and approximation of saddle-point problems arising from lagrangian multipliers,” *Revue française d’automatique, informatique, recherche opérationnelle. Analyse numérique*, vol. 8, no. R2, pp. 129–151, 1974.
- [63] J. Donea and A. Huerta, *Finite element methods for flow problems*. John Wiley & Sons, 2003.
- [64] F. Shakib, T. J. Hughes, and Z. Johan, “A new finite element formulation for computational fluid dynamics: X. the compressible euler and navier-stokes equations,” *Computer Methods in Applied Mechanics and Engineering*, vol. 89, no. 1-3, pp. 141–219, 1991.
- [65] P. Shankar and M. Deshpande, “Fluid mechanics in the driven cavity,” *Annual review of fluid mechanics*, vol. 32, no. 1, pp. 93–136, 2000.
- [66] S. K. Pandit, J. C. Kalita, and D. Dalal, “A transient higher order compact scheme for incompressible viscous flows on geometries beyond rectangular,” *Journal of Computational Physics*, vol. 225, no. 1, pp. 1100–1124, 2007.
- [67] S. Taneda, “Visualization of separating stokes flows,” *Journal of the Physical Society of Japan*, vol. 46, no. 6, pp. 1935–1942, 1979.
- [68] F. White, “Solutions of the newtonian viscous flow equations,” *Viscous Fluid Flow*, pp. 104–217, 1991.
- [69] C. Canuto, M. Y. Hussaini, A. Quarteroni, and T. A. Zang, *Spectral methods: evolution to complex geometries and applications to fluid dynamics*. Springer Science & Business Media, 2007.
- [70] M. Schäfer, S. Turek, F. Durst, E. Krause, and R. Rannacher, “Benchmark computations of laminar flow around a cylinder,” in *Flow simulation with high-performance computers II*, pp. 547–566, Springer, 1996.
- [71] D. Holdsworth, C. Norley, R. Frayne, D. Steinman, and B. Rutt, “Characterization of common carotid artery blood-flow waveforms in normal human subjects,” *Physiological measurement*, vol. 20, no. 3, p. 219, 1999.
- [72] Z. Li and C. Kleinstreuer, “Blood flow and structure interactions in a stented abdominal aortic aneurysm model,” *Medical engineering & physics*, vol. 27, no. 5, pp. 369–382, 2005.

[73] W. R. Milnor, "Hemodynamics," *Cardiac dynamics*, 1989.